

THE CARNEGIE-CHICAGO HUBBLE PROGRAM. VII. THE DISTANCE TO M 101 VIA THE OPTICAL TIP
OF THE RED GIANT BRANCH METHOD*

RACHAEL L. BEATON,^{1,†} MARK SEIBERT,² DYLAN HATT,³ WENDY L. FREEDMAN,³ TAYLOR J. HOYT,³ IN SUNG JANG,⁴
MYUNG GYOON LEE,⁵ BARRY F. MADORE,^{2,3} ANDREW J. MONSON,⁶ JILLIAN R. NEELEY,⁷ JEFFREY A. RICH,² AND
VICTORIA SCOWCROFT^{8,9}

¹Department of Astrophysical Sciences, Princeton University, 4 Ivy Lane, Princeton, NJ 08544

²The Observatories of the Carnegie Institution for Science, 813 Santa Barbara St., Pasadena, CA 91101, USA

³Department of Astronomy & Astrophysics, University of Chicago, 5640 South Ellis Avenue, Chicago, IL 60637, USA

⁴Leibniz-Institut für Astrophysik Potsdam (AIP), An der Sternwarte 16, 14482 Potsdam, Germany

⁵Department of Physics & Astronomy, Seoul National University, Gwanak-gu, Seoul 151-742, Korea

⁶Department of Astronomy & Astrophysics, The Pennsylvania State University, 525 Davey Lab, University Park, PA 16802, USA

⁷Department of Physics, Florida Atlantic University, 777 Glades Rd, Boca Raton, FL 33431

⁸Department of Physics, University of Bath, Claverton Down, Bath, BA2 7AY, United Kingdom

⁹50th Anniversary Prize Fellow

ABSTRACT

The *Carnegie-Chicago Hubble Program* (CCHP) is building a direct path to the Hubble constant (H_0) using Population II stars as the calibrator of the SN Ia-based distance scale. This path to calibrate the SNe Ia is independent of the systematics in the traditional Cepheid-based technique. In this paper, we present the distance to M 101, the host to SN 2011fe, using the *I*-band tip of the red giant branch (TRGB) based on observations from the ACS/WFC instrument on the *Hubble Space Telescope*. The CCHP targets the halo of M 101 where there is little to no host-galaxy dust, the red giant branch is isolated from nearly all other stellar populations, and there is virtually no source confusion or crowding at the magnitude of the tip. Applying the standard procedure for the TRGB method from the other works in the CCHP series, we find an foreground-extinction-corrected M 101 distance modulus of $\mu_0 = 29.07 \pm 0.04_{stat} \pm 0.05_{sys}$ mag, which corresponds to a distance of $D = 6.52 \pm 0.12_{stat} \pm 0.15_{sys}$ Mpc. This result is consistent with several recent Cepheid-based determinations, suggesting agreement between Population I and II distance scales for this nearby SN Ia-host galaxy. We further analyze four archival datasets for M 101 that have targeted its outer disk to argue that targeting in the stellar halo provides much more reliable distance measurements from the TRGB method due to the combination of multiple structural components and heavily population contamination. Application of the TRGB in complex regions will have sources of uncertainty not accounted for in commonly used uncertainty measurement techniques.

Keywords: distance scale — stars: Population II — galaxies: individual (M101) — galaxies: stellar content — galaxies: structure

Corresponding author: Rachael L. Beaton
rbeaton@princeton.edu

* Based on observations made with the NASA/ESA Hubble Space Telescope, obtained at the Space Telescope Science Institute, which is operated by the Association of Universities for Research in Astronomy, Inc., under NASA contract NAS 5-26555. These observations are associated with programs GO13691, GO14166, GO13737, and GO13364.

† Hubble Fellow

Carnegie-Princeton Fellow

1. INTRODUCTION

M 101 holds an important place in the history of the extragalactic distance scale. As one of the few nearby, large, and face-on spiral galaxies, M 101 was a natural stage for the testing of various distance measurement techniques. Cepheids have long been the standard tool for the extragalactic distance scale, but early attempts by Sandage & Tammann (1974) were unable to find Cepheids on their photographic plates of M 101 taken with the 200" Palomar telescope. From the non-detection of Cepheids to a limit of $B \sim 22.5$ mag in M 101, ‘the minimum modulus is rather ≥ 29.0 mag’ (Sandage & Tammann 1974, their section IV,a,iii). As a result, M 101 at that time set the limit on distance determination via individual Cepheid stars using photographic plates. For at least another decade, all distances in the ladder for objects more distant than M 101 were determined via other techniques.¹

A decade after this initial work, Cook et al. (1986) published the discovery of two Cepheids from imaging acquired using CCD detectors and effectively initiated a new era for the distance ladder ($\mu=29.38$ mag). Later work by this group (Cook et al. 1989; Alves & Cook 1995) continued to discover Cepheids using largely ground-based data and produced additional refinements of the distance to M 101. As a part of the *HST* Key Project (Freedman et al. 2001), Kelson et al. (1996) discovered 29 Cepheids in the disk of M 101 with WFPC2 and determined a distance modulus of 29.34 ± 0.17 mag ($D = 7.4 \pm 0.6$ Mpc). Since that time numerous other works have addressed the distance to M 101 using Cepheids and have refined the measurement (see the compilation given in Lee & Jang 2012).

Historically, M 101 served as a useful proving ground for distance measurement techniques and as a ‘‘rung’’ in the extragalactic distance ladder. However, with the appearance of SN 2011fe (Nugent et al. 2011a,b), it has become a vital target for measuring the Hubble constant (H_0) via the modern streamlined route, e.g. that using Cepheids to anchor the SNe Ia zero point. Not only is M 101 home to the most nearby SN Ia observed with modern CCD detectors, but SN 2011fe also resides in a region of low host-galaxy extinction and has come to be a powerful probe of SNe Ia physics (e.g., see Shappee et al. 2016, and references therein). Thus, a precise distance to M 101 is an important component of the modern extragalactic distance scale.

Although Cepheids have now been discovered in more distant SN Ia hosts than M 101, the difficulty in accurately measuring them—whether due to unknown levels of extinction in dusty spiral arms, inaccurate sky-background estimates due to crowding, or limited observations because of the high cost of multi-epoch imaging, among others—has motivated SN Ia re-calibration efforts of local galaxies through independent methodologies with arguably fewer systematics. The goal of this paper is to provide an independent distance measure to M 101 using Population II stars within the context of the *Carnegie-Chicago Hubble Program: (CCHP)* (PI: Freedman 2014, G013691); an overview of this effort is given in Beaton et al. (2016, Paper I).

The CCHP is a multi-facility program aimed at building a measurement of H_0 that uses SNe Ia calibrated via a technique that is fully independent of, but parallel to the traditional Cepheid route. Our cornerstone standard candle is the Tip of the Red Giant Branch (TRGB), which is the discontinuity in the RGB luminosity function resulting from low-mass stellar evolution; more specifically, at the conclusion of the RGB stellar phase, there is a rapid onset of He-core burning that causes the stars to evolve away from the RGB to the lower-luminosity Horizontal Branch. Precision TRGB distances hinge on its application to old, metal-poor stars, which can be reliably imaged in the low-extinction, low-crowding stellar halos of galaxies, which, in turn, eliminates or minimizes uncertainties due to internal extinction, point-source crowding, and contamination by other stellar populations.

The TRGB has entirely different systematics from the Cepheid route and provides not only an independent measurement of H_0 , but a means to cross-check Cepheid-based distances. In the current era where H_0 measured via the traditional distance ladder shows discordance with that from modeling CMB anisotropies at 4.4σ this independent path is a critical step toward understanding and then reconciling the controversy (Riess et al. 2011, 2016, 2018, 2019; Freedman & Madore 2010; Freedman et al. 2012; Freedman 2017).

In Hatt et al. (2017, Paper II) we outlined our CCHP reduction techniques for measuring the TRGB, and applied it to the nearby Local Group dwarf, IC 1613. In Jang et al. (2018, Paper III), we applied and demonstrated the effectiveness of these techniques to our most distant SN Ia host galaxy (NGC 1365). We demonstrated $\sim 2\text{--}3\%$ precision in distance for both galaxies, including detailed discussions and tests of our techniques. Most recently, in Hatt et al. (2018a, Paper IV), we applied this methodology to three SN Ia host galaxies in the Virgo cluster (NGC 4424, NGC 4526 and

¹ A representative history of alternative distance estimators for the case of M 101 is vividly given in the account of Overbye (1991).

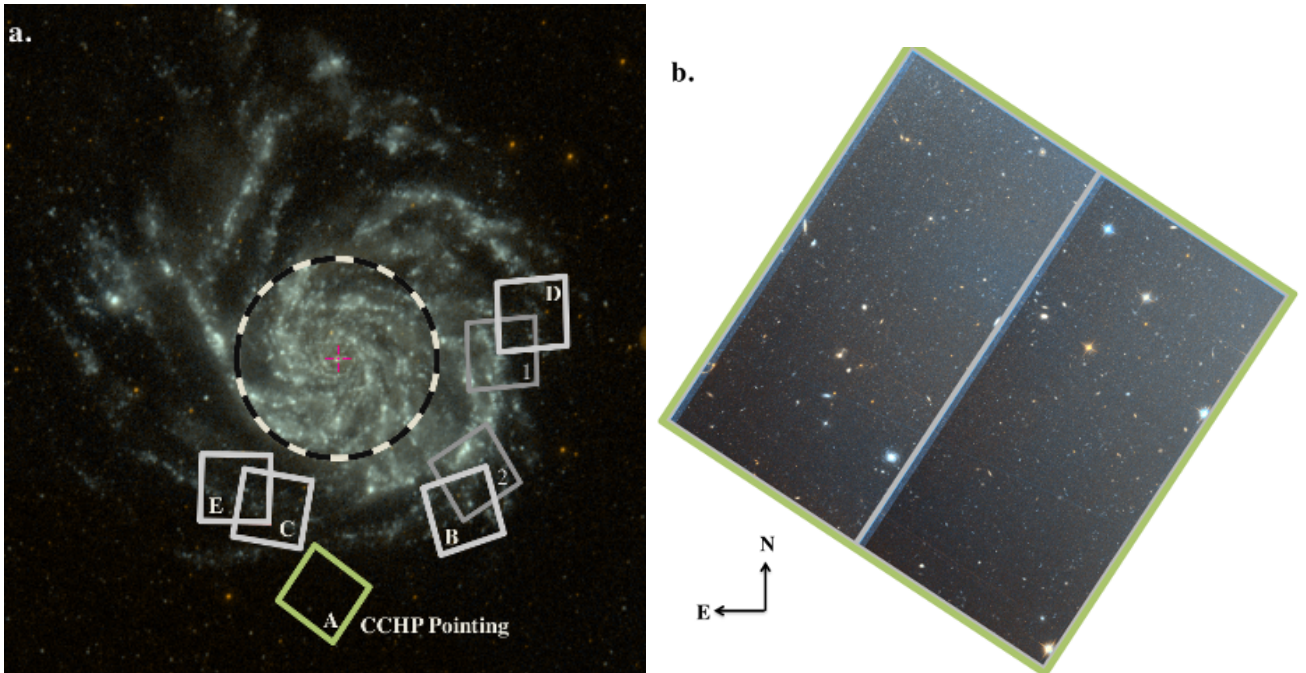


Figure 1. (a) GALEX image of M101 with the location of the CCHP Pointing indicated by a green box. The dashed-ring has a radius of 5 arcmin. Other pointings at similar radii are also shown in gray and will be discussed in section 4. The CCHP pointing is outside of the UV disk. Technical details regarding the pointings are given in Table 1. (b) Color image of the CCHP field constructed from co-added F606W and F814W images.

NGC 4536); and in Hatt et al. (2018b, Paper V), we measured the distances to NGC 1316 and NGC 1448, again with $\sim 3\%$ precision. In Hoyt et al. (AAS17233 2019, Paper VI), we applied the method to two SN Ia host galaxies in the Leo Group, again demonstrating the precision and accuracy of the technique. In this paper, we now apply these same techniques to M 101, which is the closest SN Ia host-galaxy in the CCHP. Freedman et al. (AAS17486 2019, Paper VIII), presents the final TRGB calibration and the value of the H_0 determined from the CCHP dataset.

This is not the first Population II distance to M 101. Indeed, there are five previous papers that published distance measurements that relied on the TRGB, as well as two distances in the Extragalactic Distance Database² (EDD; Jacobs et al. 2009). These distance moduli span a relatively large range, however, from 29.05 ± 0.06 (stat) ± 0.12 (sys) mag (Shappee & Stanek 2011), to 29.30 ± 0.01 (stat) ± 0.12 (sys) mag (Lee & Jang 2012), to 29.34 ± 0.08 (stat) ± 0.02 (sys) mag (Rizzi et al. 2007), to 29.42 ± 0.04 (stat) ± 0.10 (sys) mag (Sakai et al. 2004), and then most recently a value of 29.15 ± 0.04 (stat) ± 0.11 (sys) mag (Jang & Lee 2017a). In preferred distance from EDD, the is $29.13_{0.09}^{0.08}$ mag.

² he EDD is updated routinely and available at this URL: <http://edd.ifa.hawaii.edu/dfirst.php>.

Thus, while the total quoted uncertainties are of order 0.1 mag for each measurement, the spread in values is four times larger at ~ 0.4 mag. At a cursory glance, the TRGB method would seem to be relatively unreliable; though we note the spread for Cepheid distances compiled by Lee & Jang (2012) is larger, at 0.7 mag, likely due to the large number of terms in the computation of the distance (to be discussed in section 5).

As discussed in Paper I, however, the ~ 0.4 mag spread in the distance moduli from the TRGB method is most likely due to the use of fields that lie in the disk of M 101, where both crowding from neighboring sources and contamination from intermediate- and young-aged stellar populations are both a large concern for the precise and reliable application of the TRGB method. These two aspects of the pointing selection can induce strong biases in the measurement of the TRGB. In this paper, we will demonstrate explicitly the concerns with using disk-dominated fields using a set of four archival datasets. We place these archival pointings in the context of the CCHP field selection described in Paper I to demonstrate that, at the observation planning stage, one can use surface brightness profiles to bypass the confounding effects of crowding and contamination by selecting an appropriate pointing to ensure a reliable, high precision distance measurement via the TRGB.

The outline of the paper is as follows. We describe the CCHP data in section 2. We determine the appar-

ent magnitude for the TRGB of M101 and its distance from the CCHP data in [section 3](#). We perform a complementary analysis on literature fields in [section 4](#). We compare our distance measurements to other techniques in [section 5](#). A summary is given in [section 6](#). Supporting information for the data processing and analyses is provided in [Appendix A](#).

2. IMAGING AND PHOTOMETRY

The image data used in this work are described in [subsection 2.1](#). The analysis of the images to produce photometric catalogs is presented in [subsection 2.2](#).

2.1. Imaging Data

We obtained a single *HST* + *ACS* pointing in M101 at a projected radial distance of $R_{M101} \sim 23.6$ kpc ($11.6'$). The location of this pointing relative to the M101 disk is shown in [Figure 1a](#) (green box labelled M101_A). A total exposure time of 3750 s was obtained with three individual images in each of the F606W and F814W filters (G013691; [Freedman 2014](#)). [Figure 1b](#) shows a color image of the field and shows that there are no strong galactic structures (e.g., spiral arms) in the image; the use of archival GALEX imaging was particularly useful in this regard. The pointing was designed following the criteria described in [Paper I](#) to minimize contamination from non-RGB stellar populations. Full details of the pointing are given in [Table 1](#).

In addition to the CCHP field (M101_A), we also use a series of archival pointings (discussed in detail in [section 4](#)) that are also indicated in [Figure 1](#) with further specifics detailed in [Table 1](#). These data correspond to proposals G014166 ([Shappee 2015](#)), G013737 ([Shappee 2014](#)), and G013364 ([Calzetti 2013](#)), which span a range of projected radial separations ranging from 16.5 kpc to 20.2 kpc ($8.1'$ to $9.9'$). The exposure times are $\sim 1/2$ to $1/3$ of those obtained for the CCHP pointing, which makes them ~ 1 magnitude shallower. Nonetheless, these depths conform to the general signal-to-noise criteria for the CCHP targeting scheme ([Paper I](#)) and are thus ideal for testing the impact of field choice on the precision and accuracy of the TRGB measurements.

2.2. Photometry

The photometry for the five fields in M101 were processed identically using an end-to-end pipeline designed to produce homogeneous photometry for the CCHP. The pipeline was specifically designed to minimize systematic differences between photometric catalogs of different objects obtained with different integration schemes, while also providing robust measurements of systematics between frames and targets. This end-to-end approach

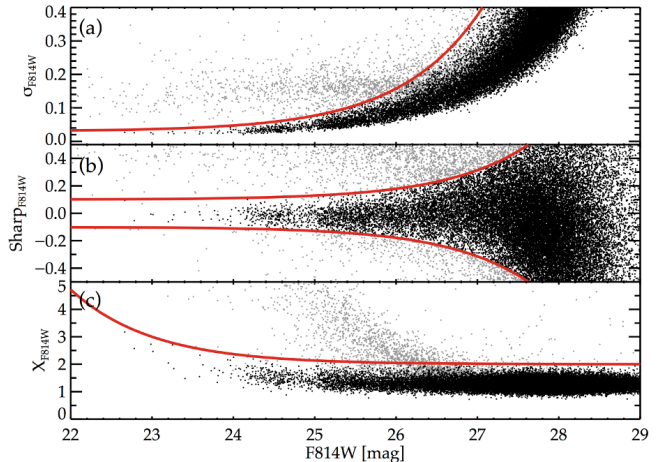


Figure 2. Photometric quality for the CCHP field (M101_A): (a) photometric uncertainty in F814W (σ_{F814W}) as a function of F814W magnitude; (b) sharp parameter from DAOPHOT as a function of F814W magnitude; and, (c) chi (χ) parameter as a function of F814W magnitude. In each panel, the solid red line is the restriction that was applied to the data to isolate stellar sources, the black points are those sources that pass all three parameter cuts, and the gray points are those sources that fail at least one of the cuts. The strong increase in source density near $F814W \sim 25$ mag marks the TRGB and we note that only a handful of sources are marginal at these magnitudes.

specifically allows for the investigations to be undertaken both globally in the CCHP and specifically in our comparison of fields in M101.

We performed photometry on the STScI processed and charge-transfer-efficiency-corrected individual frames (the FLC data type) retrieved from the Mikulski Archive for Space Telescopes (MAST) for each of the five datasets used in this work ([Table 1](#)). Detailed discussions of the CCHP data processing have been given in [Paper II](#) and [Paper III](#) in application to measurements in IC 1613 and NGC 1365, respectively. In our previous papers (e.g., [Paper II](#), [Paper III](#), [Paper IV](#), and [Paper V](#)), the photometry was implemented in a “manual” fashion, whereas the photometry used in [Paper VI](#), this paper ([Paper VII](#)), and [Paper VIII](#) were produced by an end-to-end pipeline. This pipeline is very similar to the manual analyses, but it requires no human intervention and minimizes systematics between fields caused by human choice. On the other hand, the pipeline process also eliminates field-by-field optimization as a result of human intervention. The general procedures are identical, albeit in some aspects our automated algorithmic approach necessitated both slight adjustments to our aperture core correction procedure and an implementation of sigma-clipping in our mean magnitude computations. In the remainder of this sec-

Table 1. HST+ ACS/WFC Imaging Used in this Work

Name	α^a	δ^a	r_{M101}		Program	Total Exposure Time (s)		
	(J2000)	(J2000)	arcmin	kpc ^b		F555W	F606W	F814W
M101_A	14:03:18.800	+54:09:21.00	11.6	23.6	GO13691 (PI: Freedman)		3750	3750
M101_B	14:02:30.166	+54:13:35.58	9.6	19.5	GO14166 (PI: Shappee)	1884		1491
M101_C	14:03:33.459	+54:13:24.88	8.1	16.5	GO13737 (PI: Shappee)	1170		2138
M101_D	14:02:06.461	+54:23:22.65	9.9	20.2	GO13364 (PI: Calzetti)		1130	1420
M101_E	14:03:45.960	+54:14:24.30	8.2	16.6	GO13364 (PI: Calzetti)		1100	1400

^a Field center may vary between different exposures.

^b Based on NED center (14:03:12.5441, +54:20:56.220) and NED mean distance ($\mu=29.18$ mag or 6.997 Mpc).

tion, these changes will be presented in detail within the context of our methodology.

We used the DAOPHOT family of programs to perform point-spread-function (PSF) fitting photometry (Stetson 1987; Stetson & Harris 1988; Stetson 1990, 1994). Instead of fitting an empirical PSF to the data, we create a grid of synthetic PSFs from TinyTim (Krist et al. 2011) and use DAOPHOT to fit an appropriate empirical model. The same PSF model was used for all frames of the same filter across our program. A master source list was constructed from an aligned and co-added image built from all of the images, regardless of filter, for a given pointing (using MONTAGE2). This master source list was then used in ALLFRAME to photometer each of the individual frames simultaneously.

After the instrumental photometry was computed, we determined an aperture correction for the core of the PSF (ApCore) following the calibration instructions of Sirianni et al. (2005). This was measured by comparing the magnitudes determined from the PSF photometry to the magnitudes in a $0''.5$ aperture for high signal-to-noise stellar sources in the image. Our pipeline implementation of this process differed slightly from that in our previous papers in two ways: (i) The ApCore correction is measured individually for each chip of each frame instead of a single average value computed from an image sequence and (ii) we applied a standardized selection of suitable high signal-to-noise sources instead of a by-eye evaluation. Our selection methodology compared the curve-of-growth for a source against the full range of curves of growth from our PSF grid to remove unsuitable sources. We removed flux contamination from neighbors using star subtraction routines in DAOPHOT and retested the profiles. The ApCore correction was then measured as the uncertainty weighted mean of the sources passing these criteria. Because we are determining this correction on a frame-by-frame basis, we generally had fewer stars and thereby larger uncertainties on the mean for

the ApCore than in previous CCHP works. When we visualized the ApCore measurements as a function of image number, we found that the measurements for the two chips move together systematically, which suggests that we were measuring real differences to the PSF during the observation sequence. As a result, we think that we are making a better measurement of the ApCore by calculating the correction on a frame-to-frame basis.

After the application of the ApCore for each frame, the mean magnitude for each source was determined using uncertainty weighting and a σ -clip algorithm (at 2σ). The latter is another feature of the CCHP pipeline that was not implemented in previous reductions that employed an uncertainty-weighting scheme that used all measurements for a given source. The final DAOPHOT image quality parameters, χ and sharp, were then determined as the median value reported for those frames contributing to the mean magnitude for a given source. We found that the σ -clipping produces uncertainty and image-quality parameters as a function of magnitude that had the same general shape as those from individual frames whereas those without σ -clipping often had behavior that does not track individual frame expectations. A consequence of the σ -clipping, however, were less well populated catalogs, especially on the faint end, but we are more confident in our ability to assess the photometry across the color-magnitude diagram with this modification.

The instrumental magnitudes were then put onto the STScI photometry system following the description given in Sirianni et al. (2005). The specific photometric zeropoints were retrieved on an observation-by-observation basis from the online zeropoint database³, which included updates to the zero points over time (e.g., Mack et al. 2007). Following discussion in Sirianni et al. (2005), we adopted a conservative 2% system-

³ <https://acszero-points.stsci.edu/>

atic uncertainty in flux (0.02 mag) for these zero-points. The 0'.5 to infinite aperture corrections (APInf) were adopted from Bohlin (2016) and were converted from the encircled energy (EE) tables into magnitudes. Consistent with previous CCHP papers, we adopted a 2% flux uncertainty in these values (0.02 mag; see Paper III, for a detailed discussion). We provide the values of these corrections explicitly for each field in Appendix A (Table 3).

Our final catalogs were cleaned using a series of photometric quality cuts that are demonstrated in the panels of Figure 2; more specifically, the photometric uncertainty (σ_{F814W}) in Figure 2a, the sharp-parameter (sharp_{F814W}) in Figure 2b, and the chi-parameter (χ_{F814W}) in Figure 2c. We used a constant+exponential function for each of the photometric uncertainty, sharp, and χ as a function of the F814W magnitude. This function is shown as the solid red line in each of the panels of Figure 2. We required that each source pass each of the three cuts, which are shown as the black points of Figure 2 with the gray points being those sources that fail one or more of these requirements. The specific functional form and parameters for each restriction of the photometry are given in Appendix A.

3. THE TIP OF THE RED GIANT BRANCH

The TRGB is the truncation of the RGB sequence due to the lifting of degeneracy in the core of an RGB star when it reaches a specific temperature, corresponding to a critical core mass; the bolometric luminosity coming from the core is thus reasonable approximated by a constant (the He abundance has an effect). This is both empirically well defined (Lee et al. 1993; Sakai et al. 2004; Rizzi et al. 2007, among others) and theoretically supported (Madore & Freedman 1999; Serenelli et al. 2017, among others). Naturally, the energy output from the core is modulated by the composition of the stellar atmosphere as a function of wavelength, which gives rise to the shape of the TRGB in color-magnitude diagrams. In the optical, higher metallicity corresponds to a progressively steeper, downward-sloping TRGB as incident radiation is “blanketed” in the blue and visual bands and then re-emitted thermally in the near-infrared portion of the spectrum. The slope trend of the TRGB is consequently reversed when observing in the near-infrared, i.e. higher metallicity stars appear brighter (see Hoyt et al. 2018; Madore et al. 2018). It follows that there is a transition point where the slope of the TRGB as a function of metallicity is approximately flat, or in other words, insensitive to the metal content of the stellar atmosphere. For stars that are not metal-rich ($[\text{Fe}/\text{H}] < -0.5$ dex) the Kron-Cousins I (or similar)

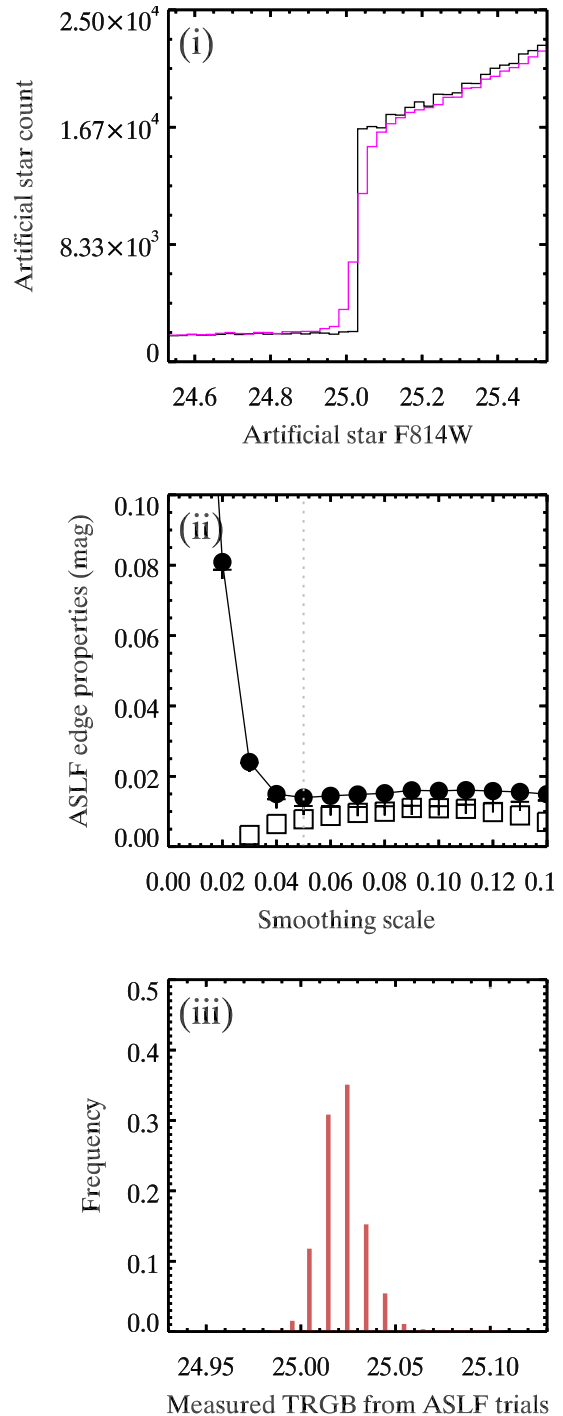


Figure 3. Uncertainties for our TRGB detection were determined via a series of simulations as described in the text for the CCHP field. (i) The input (black) and measured (purple) artificial star luminosity functions; (ii) The statistical (pluses) and systematic (open boxes) uncertainties and their quadrature sum (filled circles) as a function of σ_s for simulations of the M101 CCHP field; (iii) Distribution of measured TRGB values for our selected σ_s from which we determined the statistical and systematic uncertainties for our TRGB detection.

bandpass is in this wavelength regime where the TRGB absolute magnitude is constant with color at the few percent level (a recent detailed theoretical exploration is given in [Serenelli et al. 2017](#)); these are the types of stars that populate the stellar halo. In Pop II systems, therefore, the TRGB provides a remarkably stable standard candle that can be readily identified visually and, as described below, quantified digitally.

Detection of the TRGB discontinuity is typically done by constructing a luminosity function (LF) in the pass-band of interest by binning the marginalized apparent magnitudes. In instances where multiple stellar populations are present, the RGB locus can first be isolated in color-magnitude space using color-cuts. As has been discussed in [Paper II](#), [Paper III](#) and [Beaton et al. \(2018\)](#), there have been many different approaches to analyzing the LF to measure the TRGB. The two primary approaches are (i) the application an edge detector (to find the point of greatest change in the luminosity function) and (ii) to simultaneously fit LF models of the RGB and other stellar populations that overlap in color-magnitude space.⁴ The CCHP has adopted the former approach because it requires fewer assumptions; we do note, however, that it was shown in both [Paper II](#) and [Paper III](#) that a range of TRGB-detection methods appear consistent to within their estimated uncertainties for both the nearby and distant cases of IC 1613 and NGC 1365, respectively.

We bin the F814W magnitudes at 0.01 mag precision to construct a LF for each galaxy and then use the GLOESS smoothing algorithm to reduce the Poisson noise (a description of this algorithm is given in [Persson et al. 2004](#); [Monson et al. 2017](#); [Hatt et al. 2017](#)). One simple edge detector is the Sobel kernel $[-1, 0, +1]$, which is a discrete approximation to the first-derivative. We apply this kernel with a signal-to-noise weighting scheme and determine the TRGB magnitude as location of the greatest response in the edge detector (e.g., the point of greatest change in the GLOESS smoothed LF). The GLOESS algorithm depends critically on the user to input a characteristic kernel width that, in practice, depends on both the quality of the photometry, the number of sources defining the RGB, and the level of contamination from other stellar populations. We estimate the optimal value for this smoothing factor (σ_s) from sets of artificial star experiments; we briefly describe this process for M101 and the results are given

in [Figure 3](#) for the CCHP field. Motivations for this approach to both determining σ_s and its associated uncertainties are given in [Paper II](#).

3.1. Determining σ_s for the GLOESS Algorithm

First, we build an idealized LF with a discontinuity or ‘jump’ in star counts to model the TRGB. The LF itself consists of two components: an RGB and an AGB sequence. We assume the RGB and AGB LFs have slopes of 0.3 dex and 0.1 dex, respectively. The input TRGB magnitude itself (i.e. the start of the RGB sequence) is assigned using a preliminary measurement from the real dataset. Our RGB LF is designed to extend a full magnitude below the TRGB, while the AGB sequence starts a full magnitude brighter than the TRGB and continues uninterrupted to the bottom of the RGB sequence.

From this input LF, artificial stars are inserted into the CCD images in batches of 2000 stars. Colors are assigned to each source from a uniform sampling whose central color is the measured mean of the RGB (approximately $F606W - F814W = 1.25$ mag) and whose span is the full-color-width of the RGB (approximately $F606W - F814W = 0.5$ mag). The spatial coordinates of the sources (X, Y) are drawn from a uniform distribution and due to the small number of sources per simulation (2000) these do not strongly change the local crowding at any point in the frame. The full photometry process described in [subsection 2.2](#) is performed. This process is repeated to generate at least 1 million artificial stars, which together make an “artificial star luminosity function” (ASLF, hereafter). [Figure 3\(i\)](#) gives the input (black) and output (purple) LF for the CCHP field and demonstrates how the sharp input function is rounded by sources of noise in the returned photometry.

To characterize the statistical (random) and systematic uncertainties associated with our TRGB measurement, we model the real CMDs as closely as possible. We thus down-sample the ASLF to match the LF-statistics in our frame in a series of trials (e.g., the number of stars in broad bins across the LF). For each trial, we apply GLOESS with a single smoothing factor (σ_s) and apply the Sobel edge-detector. We repeat this process over a range σ_s varying from 0.01 mag (no smoothing) to 0.13 mag in 0.01 mag steps for 10,000 trials at each value. Using the distribution of results for each σ_s , we determine a statistical uncertainty (the distribution of measurements) and a systematic uncertainty (the mean offset from the input value). The results of this process are given in [Figure 3\(ii\)](#), which shows the run of systematic (open square), statistical (pluses), and total uncertainty (filled circles) with σ_s .

⁴ These methods typically include include thermally-pulsating asymptotic giant branch stars (TP-AGB) brighter than the TRGB and early-type AGB running parallel to the RGB, although other populations can be present.

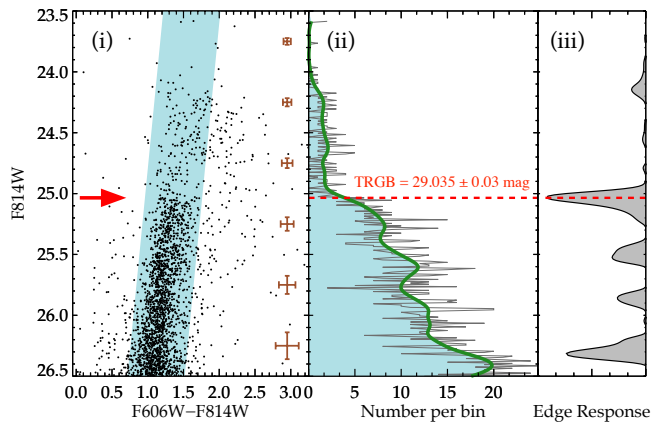


Figure 4. Detecting the TRGB discontinuity in M101. (i) CMD of the CCHP field (M101_B) with the color selection box in blue and the median magnitude and color uncertainties shown on the right side of the panel. (ii) The raw LF in bins of 0.01 mag is shown in gray with the GLOESS smoothed histogram (for $\sigma_s = 0.05$ mag) overplotted in green (and filled blue). (iii) The signal-to-noise weighted Sobel kernel response has a peak at 25.04 mag, indicated in the red dashed line. The peak of the response function is also shown in (a) as the arrow and in (b) as the red dashed line. We confidently detect the TRGB at $25.04 \text{ mag} \pm 0.03 \text{ mag}$.

We select the optimal σ_s as that value that produces the smallest total uncertainty (the quadrature sum of the statistical and systematic uncertainties) and, thereby, provides the most reliable measurement of the TRGB discontinuity. The distribution of values for our chosen σ_s is given in Figure 3(iii) and the statistical and systematic uncertainties are $\sigma_{stat} = 0.03$ mag and $\sigma_{sys} = 0.04$ mag, respectively. We note that these uncertainties are similar in magnitude to those originating from the calibration of the photometry described in subsection 2.2.

3.2. Measurement of the TRGB Distance

Having determined the optimal smoothing scale and its measurement uncertainties for our field, we now can measure the apparent magnitude of the TRGB. This process is shown in the panels of Figure 4. Our color magnitude diagram (CMD) is shown in Figure 4i with the median F814W magnitude and F606W-F814W color uncertainties shown on the right side of the panel. Following Paper II, the raw LF, binned at 0.01 mag, is shown in gray in Figure 4ii with the GLOESS smoothed result overplotted (dark green). In Figure 4iii, we apply the Sobel edge-detection algorithm and find the maximal response at, which is also indicated in Figures 4i and 4ii. Based on this analysis, we detect the TRGB at $25.04 \text{ mag} \pm 0.03 \text{ mag}$ in the F814W filter.

3.2.1. Galactic Extinction

We determine the reddening due to the Milky Way foreground using the online IRSA Galactic Dust Reddening and Extinction tool⁵ that queries the underlying Schlegel et al. (1998) maps and provides the Schlafly & Finkbeiner (2011) rescaling for a location and radius of interest. We use the central coordinate of the CCHP field and use the average reddening, finding $E(B - V) = 0.0086$ mag over a region $5'$ in diameter (Schlafly & Finkbeiner 2011). Converting into the ACS filter system via Cardelli et al. (1989), we find 0.024 mag for F606W and 0.016 mag for F814W, or $E(\text{F606W} - \text{F814W}) = 0.008$ mag. Applying the foreground estimates to our TRGB measurement from the previous subsection, we find a foreground extinction-corrected TRGB magnitude of $F814W = 25.02$ mag. Because the uncertainty in the color excess ($\sigma_{E_{B-V}} \approx 0.03$ via Schlegel et al. 1998) is comparable to the reddening, we adopt half of the reddening as an additional systematic uncertainty.

We note that the reddening for M101_B is marginally lower than the value at the center of M101, where $E(B - V) = 0.018$ mag (Schlafly & Finkbeiner 2011). Using NED, the central extinctions are $A_{F606W} = 0.051$ mag and $A_{F814W} = 0.031$ mag, which implies $E(\text{F606W} - \text{F814W}) = 0.020$ mag. These differences are, however, within the $E(B - V)$ uncertainties of Schlegel et al. (1998) and within our estimate of the uncertainty at the position of our field.

3.2.2. Internal Extinction

Reddening internal to our M101 field is unknown, although there is some evidence for internal reddening in halos (e.g., starting with Zaritsky 1994). More recently, Peek et al. (2015) used galaxies located behind stellar halos as “standard crayons” and was able to make a statistical assessment of the mean color-excess in stellar halos for galaxies at $z \sim 0.05$ as a function of projected radius. The Peek et al. analysis resulted in a reddening profile that varied from 10 to 0.05 milli-magnitudes in $g - r$ over projected distances of 30 kpc to 1 Mpc. The CCHP Field, however, is just internal to this profile, but the Peek et al. analysis places a constraint on the likely reddening at the level of ~ 0.01 mag.

On the other hand, the technique employed by Peek et al. is statistical — averaging the colors of many background galaxies and the specific properties of many host galaxies — and, thus, it is not immediately evident how to use this result in application to a specific field in a specific galaxy. In particular, there is not a good sense for the statistical distribution of dust in the halo, which could take two forms: (i) the filling factor of the dust

⁵ <http://irsa.ipac.caltech.edu/applications/DUST/>

in a full two-dimensional sense (e.g., the specifics of our pointing) and (ii) the variance of the reddening as a function of host-galaxy properties (e.g., the specifics of M 101).

In [Paper III](#), [Paper IV](#), and [Paper V](#), we tested for the impact of halo reddening by dividing the *HST* +ACS pointing into subsections, detecting the TRGB in each, and evaluating differences in the measured TRGB magnitude, which could, in principle, be interpreted as being due to extinction differences across the field. Unfortunately, we do not have sufficient source density in the M101_A pointing to perform this test with rigor (i.e., the results are consistent within the noise). Based on the narrow RGB sequence in comparison to the color-uncertainties ([Figure 4](#)), we suspect any reddening gradient to be small.

Thus, we have a potential systematic in our measurement, but one that we can anticipate to be small based on our data. We adopt an additional systematic uncertainty of 0.01 mag, based on the analysis of [Peek et al. \(2015\)](#) for their innermost bin, for the contribution of internal extinction in M 101.

3.2.3. TRGB Absolute Magnitude

From [Paper II](#) to [Paper V](#) in the CCHP series, a provisional value of $M_I^{\text{TRGB}} = -4.029 \pm 0.011_{\text{stat}} \pm 0.041_{\text{sys}}$ mag determined in the Large Magellanic Cloud was adopted (note a slight adjustment was made in [Paper IV](#) to better reflect the extinction as estimated in [Hoyt et al. \(2018\)](#)). In [Paper VIII](#), a full re-analysis of the zero-point is presented, which includes a term for the *I* to *F814W* filter transformation. The zero point is $M_{F814W}^{\text{TRGB}} = -4.049 \pm 0.022_{\text{stat}} \pm 0.039_{\text{sys}}$ mag [Paper VIII](#).

This TRGB absolute magnitude is broadly consistent with other TRGB calibrations (e.g., [Rizzi et al. 2007](#); [Jang & Lee 2017b](#), among others), with that determined from Galactic globular clusters ($M_I^{\text{TRGB}} \approx -4$ mag), and with the CCHP provisional value used in previous papers in this series. The ultimate goal of the CCHP is to use *Gaia* trigonometric parallaxes to set a direct calibration of the absolute luminosity of the TRGB following the plan outlined in [Paper I](#).

3.2.4. CCHP Distance to M 101

Combining all of the terms determined in the previous subsections, we find a distance modulus to M 101 of $\mu_0 = 29.07 \pm 0.04_{\text{stat}} \pm 0.05_{\text{sys}}$ mag, or a distance of $D = 6.52 \pm 0.12_{\text{stat}} \pm 0.15_{\text{sys}}$ Mpc. [Table 2](#) summarizes the components of the distance and the associated uncertainties.

3.3. Stability of the Edge-Detection

Table 2. TRGB Distance and Error Budget to M 101

Parameter	Value	σ_{ran}	σ_{sys}
TRGB F814W magnitude	25.04	0.03	0.04
A_{F814W}	0.02	...	0.01 ^a
M_{F814W}^{TRGB}	-4.049 ^b	0.022 ^b	0.039 ^b
True distance modulus [mag]	29.07	0.04	0.05
Distance [Mpc]	6.52	0.12	0.15

^aTaken to be half of A_{F814W} and including a 0.01 mag component from internal extinction.

^b[Freedman et al. \(AAS17486 2019\)](#)

The total number of stars at our TRGB detection is relatively small compared to previous papers in this series and it is not unreasonable to question if our chosen smoothing scale could be influencing our result. To test for the impact of smoothing, we smooth the the raw luminosity function with a range of smoothing factors from $\sigma_s = 0.02$ mag to $\sigma_s = 0.14$ mag, apply our edge-detection kernel, and determine the TRGB magnitude from the peak of the response function. In several previous works the response function has been labeled “ η ”, with the peak of the function being η_{max} and the magnitude of the peak being $m_{\eta_{\text{max}}}$ and for clarity we will use this nomenclature in the discussions to follow (e.g., starting with [Lee et al. 1993](#); [Madore & Freedman 1995](#)). The panels of [Figure 5](#) visually summarizes the result of this process, with [Figure 5a](#) being the progressively smoothed LF, [Figure 5b](#) showing η , [Figure 5c](#) a zoom into η near $m_{\eta_{\text{max}}}$, and [Figure 5d](#) exploring quantitative measures of the precision of $m_{\eta_{\text{max}}}$. Each of these panels will now be discussed in detail.

In [Figure 5a](#), the raw LF is shown in black, with the smoothed LF shown progressing from purple ($\sigma_s = 0.01$ mag) to red ($\sigma_s = 0.14$ mag). [Figure 5a](#) vividly demonstrates how the GLOESS algorithm progressively dampens the Poisson noise while also maintaining the broad features of the LF. We can anticipate that η will also show fewer noise spikes with increasing σ_s .

Indeed, [Figure 5b](#) shows η for the range of σ_s following the same color-coding as in [Figure 5a](#) and demonstrates how the numerous noise spikes are suppressed with σ_s . This suppression occurs *without losing resolution in the LF* as would occur from using larger bin-widths. From inspection of [Figure 5b](#), however, we can see that the dominant peak, at $m_{\eta_{\text{max}}} = 25.04$ mag, stays at nearly

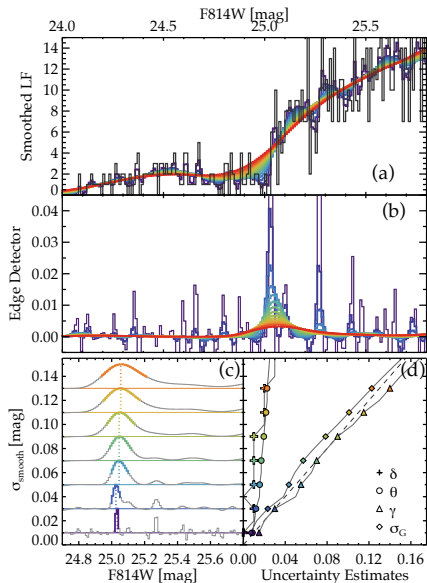


Figure 5. We study the reliability of our TRGB measurement as a function of the smoothing scale σ_s applied to the luminosity function. (a) The raw LF at 0.01 mag bins (black) is smoothed with successively larger σ_s , with blue being the smallest (0.01 mag) and red being the largest (0.14 mag). (b) The edge-detection response (η) for each of the smoothed LF represented using the same color scheme as (a). (c) A zoom into the response peak (η_{max}) for a subset of σ_s where η has been normalized (grey). The full-width at half-maximum is shown thicker and color-coded as in (a). The magnitude of η_{max} , $m_{\eta_{max}}$, is indicated with a dashed vertical line for each η . (d) A comparison of different methods for estimating the precision of $m_{\eta_{max}}$ as a function of σ_s . Each symbols is a different quantitative assessment that are defined in the text: plus – offset from the CCHP measurement (δ), circle – a metric similar to the error-on-the-mean (θ) defined in the text by Equation 2, triangle – half-width at half-maximum (γ), and diamonds – dispersion for a Gaussian fit to the response function (σ_G). Taken together, the panels demonstrate that $m_{\eta_{max}}$ is determined to high precision (0.02 mag) irrespective of σ_s and that width of the response peak is not necessarily a good measure of the uncertainty on this determination.

the same $m_{\eta_{max}}$ for all of the values of σ_s , but the value of η_{max} itself decreases and the full-width of the peak becomes much broader with increasing σ_s . However, the η for all σ_s , largely, has single dominant peak that is relatively isolated and determination of $m_{\eta_{max}}$ can be considered unambiguous for all values of σ_s .

In Figure 5c, we zoom in on the x-axis to the ~ 1 mag range around $m_{\eta_{max}}$ and the normalized η for a subset of the σ_s values (e.g., such that $\eta_{max} = 0.02$ mag on the y-axis for all σ_s). For each σ_s , η is plotted in grey and η_{max} is indicated with a vertical dotted line. From visual inspection, $m_{\eta_{max}}$ changes very little over the 0.14 mag range of σ_s . The thicker colored portion of

each response function illustrates the half-width at half maximum of the response peak (γ , hereafter), which becomes progressively broader with σ_s . In summary, we find little to no change in the $m_{\eta_{max}}$ with σ_s , although the value of η_{max} decreases and the width of the response peak (γ) broadens with σ_s . We quantify these observations in the following subsection.

3.4. Uncertainties on the Peak Magnitude

The panels of Figure 5 are designed to study the impact of σ_s on the TRGB measurement for the CCHP field. Here we define and explore several quantitative metrics that attempt to measure the precision of $m_{\eta_{max}}$ from η itself, rather than from simulations.

In Figure 5d, the half-width at half-maximum, γ_{σ_s} hereafter (demonstrated visually in Figure 5c) is plotted against σ_s with the triangle symbols (lines connect the symbols to guide the eye). Comparing the triangle symbols against the dashed one-to-one line, it is apparent that γ_{σ_s} is strongly correlated with σ_s . The dispersion of a Gaussian profile fit to the η near η_{max} (σ_{G,σ_s} hereafter) is shown by the diamond symbols in Figure 5d. Unsurprisingly, σ_{G,σ_s} is also strongly correlated with σ_s . Both γ_{σ_s} and σ_{G,σ_s} have been used in the literature to characterize the uncertainty $m_{\eta_{max}}$ directly from the edge response function, η (and in consequence the precision of the TRGB determination).

In Figure 5d, the plus symbols show the absolute difference between the TRGB at the optimized smoothing scale of $m_{\eta_{max}}$ and that measured for a given σ_s (δ_{σ_s} , hereafter). Mathematically, the term is

$$\delta_{\sigma_s} = |m_{CCHP} - m_{\eta_{max}}(\sigma_s)|, \quad (1)$$

where m_{TRGB} is the CCHP TRGB magnitude ($m_{TRGB} = m_{\eta_{max}}(0.05) = 25.04$ mag) and $m_{\sigma}(\sigma_s)$ is the peak of the response function for σ_s . The maximum value of δ_{σ_s} is 0.02 mag and it shows no correlation with σ_s .

The circle symbols in Figure 5d are a term (θ hereafter) that mimics the computation of the error on the mean. More specifically, it is the full-width at half-maximum divided by the square root of the total number of counts contributing to the peak in the LF. Mathematically, θ is defined as follows:

$$\theta_{\sigma_s} = \frac{\gamma_{\sigma_s}}{\sqrt{\sum_{\gamma_-}^{\gamma_+} (N_{*,i})}}, \quad (2)$$

where γ_{σ_s} is the half-width at half-maximum of the response peak, and $N_{*,m}$ is the value of the LF at bin i , and γ_- and γ_+ define the magnitude bin for the half-width at half-maximum brighter and fainter than the peak, respectively. From inspection of Figure 5d, θ_{σ_s} is

also uncorrelated from σ_s for the CCHP field. Moreover, this term is much more similar to the values of the statistical uncertainty that we obtain from the ASLF simulations than either γ_{σ_s} or σ_{G,σ_s} .

We can compare these different means of assessing the uncertainty of the peak detection to the values determined from our ASLF procedure (subsection 3.1). For the optimized σ_s , the statistical uncertainty is $\sigma_{stat} = 0.03$ mag and the systematic uncertainty is $\sigma_{sys} = 0.04$ mag. The δ term, which measures the difference of the response peak from peak in the optimized σ_s , is smaller than both our systematic and statistical uncertainty. Thus, for all σ_s we obtain a TRGB magnitude that is statistically consistent with the TRGB at the optimized σ_s . Thus, we conclude that the CCHP TRGB detection is insensitive to the smoothing applied to the LF.

In summary, we have explored the impact of GLOESS smoothing on the determination of the TRGB magnitude in the CCHP field. We measure statistically consistent TRGB values for σ_s between 0.01 mag and 0.14 mag and, thus, our measurement is not dependent on the smoothing scale. For the LF in the CCHP field, we find that the width of η near $m_{\eta_{max}}$ is entirely determined by σ_s and, as a result, this metric is not by design indicative of the precision of the TRGB determination from η (e.g., we determine the same $m_{\eta_{max}}$ to within 0.02 mags for all σ_s). The caveat to this statement being that the CCHP field has an isolated RGB locus in the CMD that translates to single dominant response peak in η . In the comparative analysis to follow in section 4, we will demonstrate that this is not always the case.

4. COMPARATIVE TRGB ANALYSIS

M101 is unique among the SNe Ia-host galaxies in the CCHP in that, owing to its proximity to the Milky Way, there is ample archival data from *HST* +ACS of comparable depth as our specially-designed pointing. Thus, in our study of M101, we have the unique opportunity to test our measurement directly on other fields and to evaluate our field selection strategy in a quantitative fashion.

We searched the *HST* archive for pointings with comparable depth and positioning, at least, in the outer disk of M101. We restricted our search to ACS/WFC pointings, for which our pipeline has been optimized, and we also required F814W observations with an exposure time to attain S/N \sim 10 at the approximate magnitude of the TRGB, and limited our search to pointings with central coordinates at $R_{M101} > 5'$ and having no dwarf satellite in the frame. Applying these conditions to the available imaging in the *HST* archive, there were six suitable im-

age datasets (not including the CCHP Field). All six additional pointings are shown with the CCHP Field in Figure 6a; these data are from GO14166 (Pointings C and 2), GO13737 (Pointing D), and GO13364 (Pointings E, F, and 1). The color coding in Figure 6a is coordinated with the *HST* observing program. Pointings 1 and 2 (indicated in gray in Figure 1a) are both visually dominated by spiral arms and were deemed not suitable for our goals. The remaining four were considered suitable, though not ideal, for a TRGB measurement and their observation details are given in Table 1.

First, we compare the locations of these fields to 1-D and 2-D maps of M101 in subsection 4.1. Then we compare the CMDs of the archival fields to that of the CCHP Field in subsection 4.2. A detailed TRGB detection analysis is given in subsection 4.3 and a discussion of the internal extinction is given in subsection 4.4.

4.1. Comparison to Surface Brightness Profiles

Across the CCHP, the *HST* +ACS imaging fields were selected based on a set of quantitative surface brightness criteria using a combination of archival *WISE* and *GALEX* imaging. More specifically, each pointing was selected to straddle the 27-28 mag arcsec $^{-2}$ isophote while also being on the 25-26 mag arcsec $^{-2}$ isophote in the *WISE*-1 band (W1). The combination of these surface brightness criteria was meant to mitigate contamination from younger populations (traced by the UV) while also having enough RGB stars to be able to make our measurement (traced by W1). Where necessary, this overall strategy was modulated to avoid extended disks (especially important for M101) and other young or tidal structures obvious in archival imaging; as a result, the fields were often positioned on the minor axis of the galaxy.

In Figure 6b, we compare the approximate locations of the five *HST* +ACS fields to *WISE*-W1 and the *GALEX*-FUV and -NUV surface brightness profiles. These surface brightness profiles were constructed similar in form to the methodology presented in the *GALEX* Nearby Galaxy Atlas (Gil de Paz et al. 2007), but were applied to custom builds of the *GALEX* and *WISE* imaging for M101. The approximate radial extent for each of the five pointings is indicated with the colored bars, with the CCHP Pointing (M101_A) spanning both the largest radial extent and being the most distant from the M101 center. Each of the archival pointings fall on visible features in the *GALEX* surface brightness profile that indicate spiral arms and, by association, contaminating young and intermediate-aged populations that could systematically bias an otherwise precise detection of the TRGB. Thus, we would predict from Figure 6a

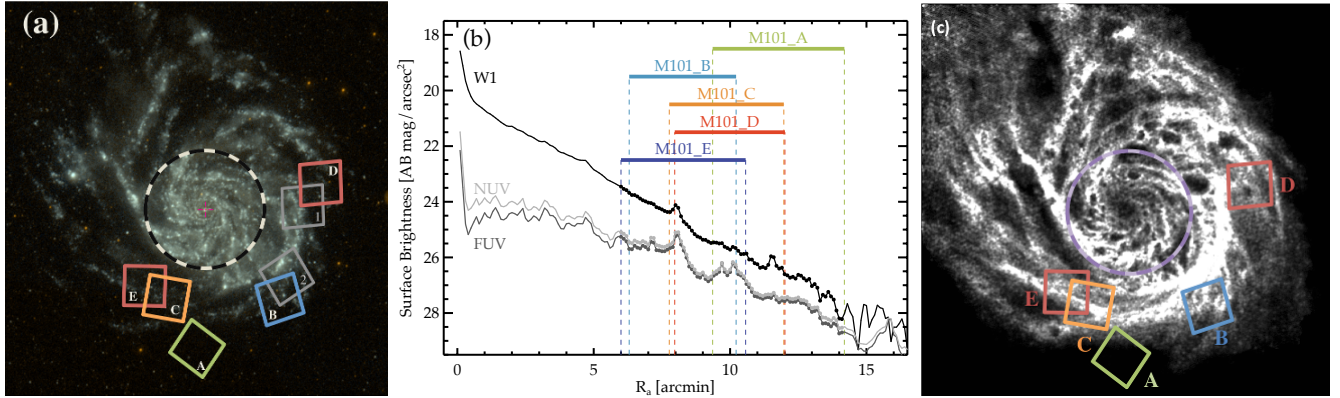


Figure 6. Location of the *HST* +ACS imaging for M101. (a) Map of *HST* ACS/WFC pointings in M101 that meet our signal-to-noise and crowding criteria for TRGB measurement (see Figure 1 for additional details). The four archival pointings (labeled B through E and color-coded by the *HST* observing program) have been analyzed identically to the CCHP Pointing. The two pointings indicated in grey (pointing 1 and 2) met our signal-to-noise requirements, but were not used due a high fraction of young stars. Technical details regarding the pointings are given in Table 1. (b) Surface brightness profiles for M101 derived from *GALEX* (NUV and FUV) and *WISE* (W1) imaging. The radial extent for the five pointings used in our comparative analysis are shown. The CCHP pointing (M101_A) was chosen to span the 25-26 mag arcsec⁻² isophote in W1 and the 27-28 mag arcsec⁻² isophote in NUV. The CMD for the CCHP pointing (M101_A; Figure 4) suggests that these quantitative criteria select for Pop II dominated regions. (c) M101 pointings used in this work overlaid on a neutral hydrogen map from THINGS (Walter et al. 2008) and retrieved from NED. The overall scale is similar to that of Figure 1a and Figure 6a with the annulus representing a radius of 5'. Only the CCHP Field is outside of the gaseous disk of M101 (to the limiting column density of the observations).

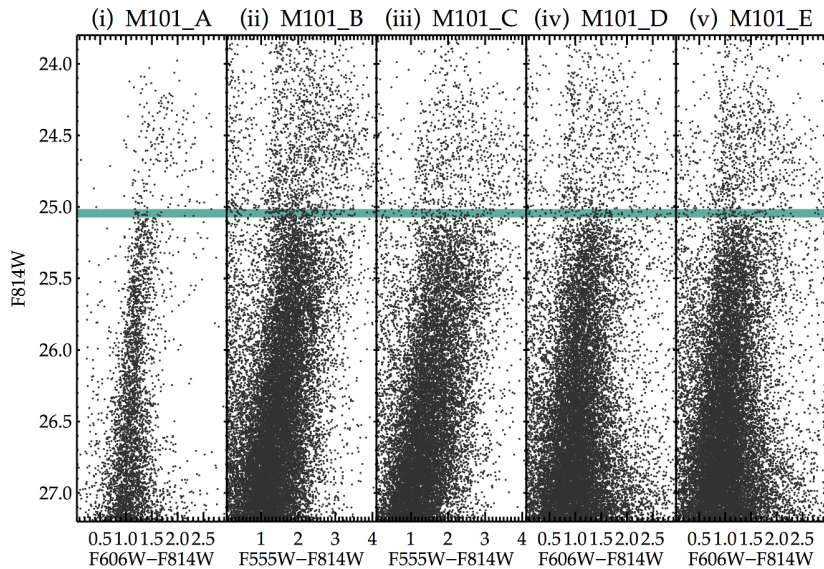


Figure 7. Color-magnitude diagrams for the five fields in the outer-disk of M101 used in this work. The panels are (i) our ‘pure halo’ pointing for the CCHP (M101_A), (ii) the M101_B pointing, (iii) the M101_C pointing, (iv) the M101_D pointing, and (v) the M101_E pointing. Note that the color in panels (i), (iv), and (v) is $F606W-F814W$ and in panels (ii) and (iii) is $F555W-F814W$, with the x-axis color range spanned by the former being transformed into the latter system as described by Equation 3. A filled band represents the TRGB discontinuity determined from M101_A with the width of ± 1 -sigma (Table 2). The difference in the stellar populations amongst the fields is visually striking and largely conforms to the placement of the pointings in relation to the spiral arms as demonstrated by Figure 6a.

and Figure 6b that the archival pointings, despite having strong RGB sequences as indicated by a higher *WISE* W1 surface brightness, will suffer from disproportionately stronger contamination by young and intermediate age populations. This contamination has the potential to make the accurate and precise measurement of the TRGB difficult, despite there being more RGB stars.

4.2. The Color-Magnitude Diagrams

The images for the archival fields were processed and photometry was produced identically to that for the CCHP field (subsection 2.2), but with appropriate modifications of the photometric zero points (these are given in Appendix A in Table 3). We restrict the photometry for each pointing using the scheme described for our CCHP field (Figure 2), but with an adjustment made, based on the photometric depth of the field, to the magnitude at which the photometric error model transitions from a constant to an exponential form (visualizations can be found in Appendix A in Figure 10 and values are given in Table 3).

Figure 7 presents the color-magnitude diagrams for each of the five fields. To compare the F555W-F814W color scales (pointings M101_B and M101_C), we transform the F606W-F814W color ranges to the approximate F555W-F814W color following the relationships defined by Jang & Lee (2017b) as follows:

$$\begin{aligned} \text{F555W} - \text{F814W} = \\ 1.393(\pm 0.003) \times (\text{F606W} - \text{F814W}) - 0.004(\pm 0.004) \end{aligned} \quad (3)$$

for stellar sources with $(\text{F606W} - \text{F814W}) < 1.5$ mag. Using the transformation, the x-axis scale for the panels of Figure 7 was modified for M101_B and M101_C such that any apparent differences on the RGB are not driven by the physical differences in the filter systems (F555W-F814W is naturally a larger color baseline than F606W-F814W). The green band in Figure 7 gives the TRGB magnitude determined for the CCHP field, with the width indicating its statistical uncertainty.

Comparing the CCHP Field (Figure 7i) to the other four fields, there are a number of noteworthy differences. First, the total number of stars is dramatically higher in the archival fields for all stellar types. Second, there are pronounced young (blue) and intermediate-aged (AGB) populations in the archival fields that are absent (or nearly so) in the CCHP field. Third, the RGB in the archival fields is much broader in color, which can be attributed to these fields sampling stellar populations with a broader range of ages and metallicities, as well as possibly being due to differential extinction within the structural components probed by these lines of sight.

The impact that these differences have on the TRGB identification is not immediately obvious from the panels of Figure 7. Visually, the discontinuities do not look significantly different from that in the CCHP field (green band), albeit these look slightly fainter. While the contaminating populations are a concern, it could be argued that the significantly larger number of RGB stars contributing to the TRGB would counterbalance the impact from the other populations. In the next subsection, we explore quantitatively why this is not the case.

4.3. TRGB Determination in Archival Fields

In demonstrating the stability of our TRGB detection for the M101_A field, we undertook an exercise of comparing the LF, edge-response, and predicted uncertainties for a range of smoothing factors. We repeated this procedure for each of the four archival fields; Figure 8 contains the summary panels for each of the fields (Figure 5c and Figure 5d) and the full visualizations are given in Appendix A, Figure 11. The colors, annotations, and axis ranges are identical between the panels and the M101_A field is repeated for ease of comparison.

A comparison of the LF for each of the fields quantifies the considerably larger number of stars in the archival fields for all magnitudes. However, while the RGB population improved by roughly a factor of 3, the contaminating AGB population increases in number by roughly a factor of 5 to 6. Nevertheless, from visual inspection the sharpest TRGB jump in the LF is in M101_A, with the archival fields showing a much more gradual transition from the AGB to RGB. The GLOESS smoothing makes the transition even more gradual but, as we observed in application to the CCHP field, it does not innately distort the LF shape.

Comparing the edge response (η) for the archival fields to the CCHP field begins to reveal how the contaminating populations impact the determination of the TRGB (Figure 8, left panels). At the smallest smoothing scales (less than 0.02 mag, dark blue/purple), the edge detection response has significantly more false-peaks occurring both brighter and fainter than the TRGB; these discontinuities are due to Poisson fluctuations in the LF. Sometimes, multiple peaks occur very near each other making the selection of the most appropriate peak difficult. On the other hand, while larger smoothing scales serve to dampen these peaks, the peaks also start to merge with each other producing composite peaks in the edge response (η) that are both non-Gaussian and asymmetric.

The consequence of the latter point is demonstrated quite clearly when comparing $m_{\eta_{max}}$ (vertical dotted lines) for each smoothing scale in Figure 8 (left panels).

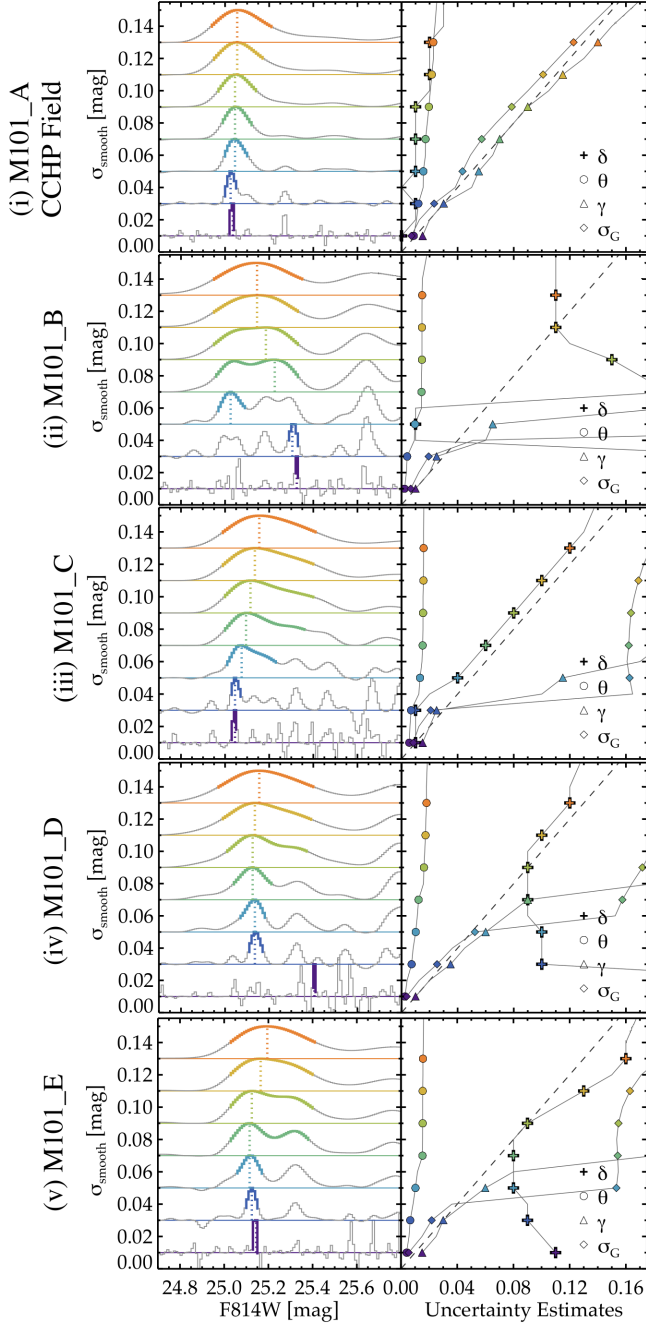


Figure 8. Edge-detections (left) and uncertainty estimates (right) as in Figure 5c and Figure 5d, respectively, for each of our five fields, from top (i) M101_A, (ii) M101_B, (iii) M101_C, (iv) M101_D, and (v) M101_E. The detection stability seen for the CCHP Field is not seen in the archival fields as their edge detection response functions are broader, multi-peaked, and asymmetric. Moreover, common metrics to define the “precision” of result via the edge response show little to no correspondence with the actual uncertainty.

The effect is most striking for σ_s of 0.06 mag and larger for M101_C and M101_D (Figure 8(ii) and Figure 8(iii), respectively), where the width of the peaks is quite asymmetric and broad (spanning nearly the full range of the figure.). Furthermore, the maximal response, itself, can shift as much as 0.3 mag across 0.01 mag smoothing shifts. In addition to sharp jumps in the maximal response with smoothing factor, we also see slow drift of the maximal response (Figure 8(iii) and Figure 8(v)) and this drift can be both to fainter or brighter magnitudes (e.g., Figure 8(ii)).

One could attribute the instability of the η_{max} to either the method or size of the smoothing. In the CCHP field, however, we show that we have a stable response for all smoothing scales, including that of “no smoothing” (Figure 8i). Stated differently, for the CCHP field the smoothing serves to clarify the result and not to bias or distort it. Instead, we attribute the source of the instability in the archival fields to the contaminating populations that have the effect of adding considerable noise to the LF both brighter and fainter than the TRGB. Moreover, we are seeing composite populations along the line of sight; while their physical separation is not resolved at the precision of our photometry, the differences in the dust column between their physical separations could produce noise spikes from bona-fide TRGB stars. This noise, in turn, can both mask the true TRGB peak and, with larger smoothing scales, “drag” the peak away from the TRGB.

Another aspect of the TRGB detection via the maximal response function is also worth mentioning. It is often argued in the literature that the “closest” TRGB stars will contribute to the peak and thus complexity along the line-of-sight is not a concern (see e.g., Shappee & Stanek 2011; Tikhonov et al. 2015, among others). As our experiment with the archival fields has shown, however, the maximal peaks most often correspond to where the “bulk” of the TRGB stars are along-the-line of sight into the galaxy. At small smoothing scales we do often get peaks at or near the “halo” pointing of M101_A, but as smoothing is incrementally applied, the peaks tend to be at fainter magnitudes, which, as previously discussed, are likely TRGB stars in the disk of M 101, are consistent with being behind some dust column, and likely comprise a more complicated mix of stellar populations than our halo sample (e.g., metallicity/age effects). We will return to this point in section 5 with respect to literature studies of M 101 applying the TRGB method.

We also note how the uncertainty estimates in the right panels of Figure 8 change with the indeterminate results in the right panels. The quantity δ defined in Equation 1 as the difference between the CCHP mea-

surement and that in an individual case behaves erratically as anticipated, with the exception of Figure 8iii and Figure 8iv, where at some point it grows in lock-step with the smoothing factor (it traces the 1:1 line in right the panels). Of note, the quantity θ (circles) defined in Equation 2 shows consistent behavior for all five panels, meaning that it is a poor measure of the distance uncertainty. Likewise, the quantities γ and σ_G seem to also perform poorly as measures of the uncertainty, as they either grossly over- or under- estimate δ , but are always equal to or larger than the smoothing scale, σ_s . At some level, however, they are representative of how reliable a heavily smoothed LF is, in that at large smoothing scales these estimates do provide 1- σ consistency with the CCHP result – this is seen in Figure 8 as δ is smaller than γ or σ_G for $\sigma_s > \sim 0.05$ mag. We conclude here in most cases, error estimates that are derived from the response function η are not reliable measures of the uncertainty with the exception of γ and σ_G in the cases of large smoothing ($\sigma_s > \sim 0.05$ mag). This does provide a cautionary note to error estimates that are significantly smaller than the effective smoothing scale of the LF, whether that smoothing is conducted by binning, smoothing of the LF, or broadening of the edge-detection kernel, in that the response η is heavily impacted by these choices.

Thus, while our original goal was to compare the measurements between archival fields and the CCHP field, we have, instead, come to the conclusion that we cannot unambiguously measure a distance to any of the archival fields at comparable certainty. Moreover, our ASLF methods that were designed to determine the “optimal” smoothing scale for measuring the TRGB and its associated uncertainties are not well suited to handle the complexity of the stellar populations in the archival fields. Thus, for rigorous, high-precision detection of the TRGB (as is our goal here), we come to the conclusion that the selection of an appropriate field is as important, if not more important, than considerations for the number of stars and the depth of the imaging.

4.4. Extinction in the Archival Fields

In the previous subsection, we used archival HST data to explore the impact of ambiguous peaks in the edge response function on the measurement of the TRGB. However we also need to consider differences in the total extinction along the line-of-sight. The extinction from the Milky Way foreground is very similar between all five fields (the exact values for each field are given in Table 3 and were determined identically to that of the CCHP field), but we must also consider the potential for additional internal-extinction within M101.

More specifically, the archival pointings look into the outer disk of M101 and thereby probe multiple structural components; in the Milky Way, a similar pointing would probe the halo (and potentially substructure) and both the thick and thin disk. An additional complication, however, will be that each of these structures will have their own associated columns of interstellar material, with the thin disk being the most likely to have appreciable amounts, while also having the largest number of stars. Taken together, we anticipate that we are most likely to trigger off of a thin disk population which would, by design, require an additional term for extinction within M101.

In comparing the TRGB identifications from the maximum response in Figure 8, the majority of the detections are just fainter than that in the CCHP field — with the exception of the small smoothing scales ($\sigma_s < 0.04$ mag) for M101.D in Figure 8(iii) and intermediate smoothing scales for M101.C Figure 8(ii). While the archival pointings are in the outer regions of M101, they are still in regions with significant UV emission (Figure 6a and 6b) and show signs of relatively young stellar populations (Figure 7).

In Figure 6c, the positions of the HST fields are overlaid on the total power HI map from the THINGS survey (Walter et al. 2008, retrieved from NED). The CCHP field (M101.A) is largely free of gas to the limiting column of the survey, which is $\sim 3.2 \times 10^{20}$ cm⁻² in the “normal” spatial resolution (Walter et al. 2008). The conversion from atomic gas to reddening is quite nuanced, especially so at the few 0.01 mag level, but that the projected locations of the archival fields are all within the gaseous disk provides circumstantial evidence of there being internal extinction for the RGB stars in the disk. Because the highest density of RGB stars along the line-of-sight is in the disk for these archival pointings, some fraction of those RGB stars will be impacted by the presence any dust associated with the HI gas. Moreover, high-quality HI maps are often available for nearby galaxies and this is an aspect of field selection that can, and should, be considered for high-precision TRGB measurements. We note that this guideline can be applied both to select new or to screen archival observations; the latter being performed in Anand et al. (2018).

Thus, the observation that most of the TRGB measurements made in the archival fields are fainter than that in the CCHP field is fully consistent with there being extinction from interstellar material in outer disk of M101. Or at least that the dominant contribution to the TRGB signal is a population of stars behind some amount of dust. Indeed, some of the ambiguity discussed in the previous section could be coming from RGB stars

in multiple structural components of M 101 behind different amounts of dust. By moving safely into the stellar halo, our TRGB measurements are less susceptible to systematic effects from dust extinction.

4.5. Discussion

In this section, images for four archival points in M 101 were processed and analyzed identically to that of the CCHP field. We demonstrated that we cannot determine a TRGB detection in any of these fields unambiguously. Moreover, we have shown that our pointings simultaneously avoid contamination from younger stellar populations and minimize interstellar extinction effects to a level below our measurement uncertainties. We posit that the quantitative field selection strategy of the CCHP has helped its success in this regard.

Qualitatively, the CCHP targeted fields in the “stellar halo.” We note that other programs used a similar selection strategy by focusing on the outer-components of galaxies (most notably, McQuinn et al. 2016a,b, 2017, among others). Inspection of these works indicate, that although these fields are outside of the traditional disk, they contain contamination from stars more luminous than the TRGB – both AGB stars or red super-giant sequences (for example M 74 in McQuinn et al. 2017). Moreover in application to M 101, we have shown that fields in its outer regions they still have an unknown, and indeed perhaps *unquantifiable*, impact from interstellar extinction. The presence of young to intermediate age populations and not insignificant extinction were anticipated in the CCHP in part due to detailed observations of the outer Milky Way disk that show these characteristics to large radii (for a brief overview see Carraro 2015).

Quantitatively, the CCHP performed targeting using wide-area, multi-wavelength surface-brightness maps from well characterized all-sky surveys. Of particular utility was placing a field that sampled a specific isophote in *GALEX* (that track young populations even to low stellar density) and *WISE* (that track the older stellar populations) using two-dimensional maps; this is demonstrated by the radially binned map shown in Figure 6b. These quantitative choices were found by a review of literature CMDs and their placement on surface-brightness maps (a good example being the CMD of NGC 4258 in Mager et al. 2008). Likewise, HI maps Figure 6c provided additional diagnostics to avoid interstellar material. The quantitative metrics demonstrated in Figure 6 were used for all galaxies in the CCHP sample (see Paper I).

5. DISCUSSION

Our primary purpose in evaluating the archival fields in this work was to understand if or how our TRGB measurement compares to other locations in M 101. We now compare these measurements to those from earlier studies. Instead of comparing the final distance moduli, we will compare the actual tip magnitudes and the locations of the fields used in each of the papers to eliminate differences in the adopted TRGB zeropoints. As demonstrated in previous discussions, the variation of the foreground Milky Way extinction across M 101 is small and unlikely to be a large concern in the comparisons to follow, whereas extinction *internal* to the component of M 101 being studied is more problematic. The distance moduli and uncertainties are visualized in Figure 9a using our TRGB zeropoint. The data used in Figure 9 is given in subsection A.6, with references to all studies not mentioned explicitly in the discussion to follow.

5.1. Summaries of Previous TRGB Studies

Sakai et al. (2004, S04) used the two outer chips of a WFPC2 pointing in the outer disk of M 101 following the data-analysis strategy of Hill et al. (1998, from the Key Project). The authors use a series of edge-detectors, including a linear LF, log LF, and a cross-correlation technique. The authors find overall consistent tip detection at $I=25.41 \pm 0.04$ mag. They comment on the field being contaminated heavily by young- and intermediate-aged populations.

Rizzi et al. (2007, R07) repeated the analysis of S04, but using the HSTPhot package (Dolphin 2000a) to produce photometry of the same fields. The authors determined a TRGB magnitude of $I_{TRGB} = 25.31 \pm 0.08$ mag, which is in rough statistical agreement with that derived by S04 (there is a $\sim 1\sigma$ difference).

Shappee & Stanek (2011, SS11) used two HST+ACS fields in the inner disk of M 101 (within the $5'$ radius plotted in Figure 6a) and determined photometry using the DOLPHOT package that is specifically optimized for crowded field photometry. Of note, DOLPHOT applies CTE corrections internally and derives its own aperture corrections. SS11 only use sources that are more than $4.75'$ in radial separation from M 101 (to reduce AGB contamination) and remove sources with $V- < 1.0$ mag (to reduce contamination both from blue AGB stars and younger populations). SS11 adopt the “continuous” form of the LF from S04, the logarithmic edge-detector from Méndez et al. (2002), and apply a Poisson-statistics based signal-to-noise weighting scheme. At its spirit this TRGB detection formulation is the most similar of the literature studies to that undertaken in our CCHP Field (M101_A). Recognizing that their field will

contain a range of metallicities, [SS11](#) translate the photometry into the T magnitude defined by [Madore et al. \(2009\)](#), a magnitude system which was designed to “remove” the downward slope of the TRGB for a multi-population RGB (a comparison of this technique and others is given [Beaton et al. 2018](#), their section 4.2.2 and figure 28). [SS11](#) obtained a tip magnitude of $T = 25.00 \pm 0.06$ mag, which is notably different from the values derived by [R07](#) and [S04](#), above.

[Lee & Jang \(2012, LJ12\)](#) re-reduced eight fields, including those used by both [S04](#) and [SS11](#). The authors consistently found a TRGB magnitudes between 25.24 and 25.30 mag with typical uncertainties of order 0.03 mag. The T magnitudes range from 25.15 to 25.33 mag with similar uncertainties. The values from [LJ12](#) are in agreement with those of [R07](#) and [S04](#), and differ by $3\text{-}\sigma$ to $5.5\text{-}\sigma$ from that of [SS11](#). These are all pointings well within the extent of the UV and gaseous disk of M 101.

In [Tikhonov et al. \(2015, T15\)](#), three *HST* + ACS fields were analyzed, one of which is M101.D. The TRGB detection in each field was as follows: F1: 25.05 mag, F2: 25.10 mag (Pointing 1), and F3: 24.11 mag (M101.D). [T15](#) provide no uncertainties and the details of the exact procedures employed in this work are more sparse than those in other literature studies discussed here. Qualitatively, these results agree with our processing in these fields. The final distance quoted by [T15](#) appears to be that of their F3, our M101.D, field, which is at the largest projected radial distance from M 101.

In [Jang & Lee \(2017b, JL17\)](#), the M 101 measurements of [LJ12](#) were revisited by the authors. [JL17](#) use the pointing we call M101.E (see [Table 1](#)) and find a TRGB magnitude of $F814W = 25.16 \pm 0.035$ mag. This is 0.12 mag brighter than the result in [LJ12](#). In their section 4.1, [JL17](#) explained the difference between this result and [LJ12](#) as being due to (i) changing the procedure for the aperture correction and (ii) having used images that were not fully corrected for the charge-transfer-efficiency. In addition, [JL17](#) note that the M101.E data was significantly deeper than that used in [LJ12](#) and had a visibly stronger TRGB signal, both of which would impact the result. [JL17](#) binned their data in 0.05 mag bins and applied a “classic” Sobel kernel ($[-1, -2, 0, +2, +1]$) to find a broad edge-response peak between 25.0 and 25.3 mag with a similar TRGB detection in both the F814W and *QT* photometric systems; the latter is a variant of the T system that incorporates a quadratic color-term (a comparison of this technique and others is given [Beaton et al. 2018](#), their section 4.2.2 and figure 28).

Lastly, the Extragalactic Distance Database (EDD [Jacobs et al. 2009](#)) presents a TRGB-based distance using two CMDs.⁶ The two CMDs are derived from data taken on *HST* via programs GO 9492 (PI: Bresolin) and GO 13691 (PI:Freedman, the CCHP field). The preferred TRGB detection for the EDD is 29.08 mag. The EDD uses either HSTPHOT or DOLPHOT for WFPC2 or ACS, respectively to produce CMDs to which the [Makarov et al. \(2006\)](#) Maximum-Likelihood algorithm is applied and the [R07](#) zero-point is adopted.⁷

Given the data processing discrepancy identified by [JL17](#) in [LJ12](#), the data analysis techniques for [S04](#), [R07](#), and [SS11](#) were carefully reviewed to determine if the large range of distance moduli found in these works could be understood relative to data processing choices. [S04](#) follows the [Hill et al. \(1998\)](#) photometry prescription, which does not employ a CTE correction, and adopts aperture corrections from distinct *HST* observations, more specifically those corrections determined in observations of the dwarf galaxy Leo I presented in [Hill et al.](#) The differences between the more crowded M 101 field as well as telescope “breathing” or other PSF modulations mean that these aperture corrections may not be well suited to the M 101 data. Thus, the [S04](#) result, which is the largest TRGB-based distance modulus, could be attributed to these aspects of the data processing.

On the other hand, [R07](#) analyzed the [S04](#) field using the HSTPHOT code, a precursor to DOLPHOT that operates on similar underlying techniques in terms of “native” PSF modelling, application of CTE corrections, and determination of aperture corrections ([Dolphin 2000a,b](#)). The [R07](#) TRGB agrees with that of [LJ12](#) that used the WFPC2 module for the later DOLPHOT code, which should operate under similar principles, but is still more distant than results from *HST* +ACS at the ~ 0.2 mag level (10% in distance). That these latter two studies produce statistically indistinguishable results despite performing independent analyses, does suggest that there is something intrinsic to either this field or this dataset. We therefore suspect, as was discussed in [JL17](#), that the depth of this WFPC2 pointing or something other characteristic about its location

⁶ The data for M 101 can be found at the following URL: http://edd.ifa.hawaii.edu/get_cmd.php?pgc=50063, which presents the visualizations associated with the “CMDs/TRGB” entry for M 101.

⁷ This text is adapted from the EDD “CMDs/TRGB” description, which can be found on its main page, e.g., <http://edd.ifa.hawaii.edu/>

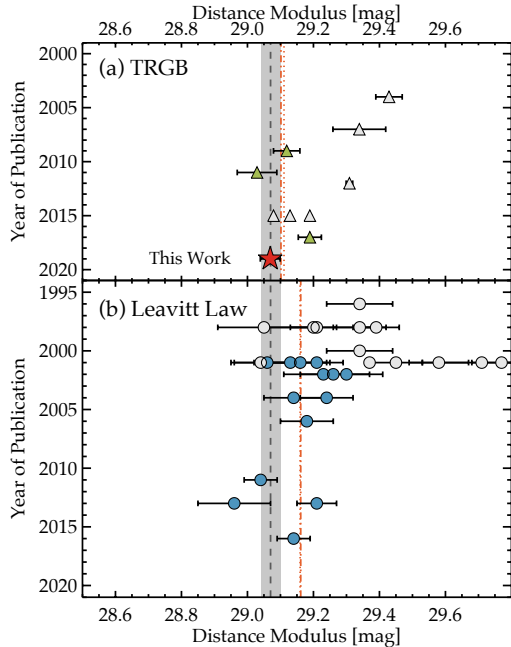


Figure 9. Comparison of literature distances to M101 using (a) the TRGB and (b) the Leavitt Law for Cepheids. In both panels, the value for the CCHP and its statistical uncertainty are shown as the dashed line and gray band, respectively. For the TRGB measurements, we have homogenized the absolute magnitude of the TRGB to the value used in our work. For the Leavitt Law distances, the values were compiled from NED (Steer et al. 2017) and no homogenization has been applied owing to the numerous terms that need to be taken into account, although we have attempted to use those on an LMC-based scale for consistency with the TRGB. In each panel, the red dotted line and dot-dashed lines show the uncertainty weighted and unweighted means, respectively, based on the filled symbols (green for the TRGB and blue for the Leavitt Law). See the text for more discussion.

within M101 is the likely source of the “long” TRGB distances to M101 measured by S04, R07, and LJ12.

5.2. Detailed Comparison to JL17

The TRGB detection of JL17 of $F814W = 25.16 \pm 0.035$ mag, despite having similar statistical uncertainties, is $3\text{-}4\sigma$ from the result in the CCHP field; even considering our total uncertainty, there is still a non-negligible difference between these results. However, this result uses the M101.E field that was included in our archival analyses and, thus, we are able to do a detailed comparison to JL17 and attempt to understand the origin of the discrepancy. Additional supporting descriptions and figures are given in subsection A.5.

With the caveats of subsection 4.3 in mind, we repeat the ASLF procedure for the M101.E using our best estimation of the LF. We selected the optical smoothing

factor as the value that minimizes the combined uncertainty, which occurs at $\sigma_s = 0.05$ mag. The corresponding statistical and systematic uncertainties are 0.03 mag and 0.04 mag, respectively; we note, however, that owing to the complexity of modeling the non-RGB and non-AGB stellar populations contributing to the LF these likely represent lower limits on the uncertainties. We applied a color-cut to the CMD that is defined by the CCHP Field (M101_A), but broadened commensurate with the larger photometric uncertainties for this field; JL17 also apply a color cut in their analysis. The result is a TRGB detection at 25.105 ± 0.03 mag, though we note that the detection peak is asymmetric, but the asymmetry does not distort the result. Moreover, from Figure 8(v), both narrower and broader smoothing windows trend toward a measurement closer to 25.15 mag, albeit with larger uncertainties. The foreground extinction to this field is $0.01 \text{ mag} \pm 0.01 \text{ mag}$ such that the extinction corrected tip is 25.10 ± 0.03 (stat) ± 0.04 mag (sys). This result sits in between the measurement from JL17 and that from the CCHP field (M101_A) and its uncertainties, taken together, are $1\text{-}\sigma$ consistent with either result. From this, we conclude that the difference in the distance measurement between this work and JL17 is dominated by the field choice, with differences in the underlying data processing or analysis playing a sub-dominant effect.

5.3. Comparison to Cepheid Distances

There are numerous Cepheid distances to M101 and those distances published since the Key Project are compared in Figure 9b. The distances were retrieved from NED and no homogenization has been applied owing to the complexities therein. We do note that the bulk of the studies use the Key Project distance modulus to the Large Magellanic Cloud of 18.50 mag (Freedman et al. 2001), which has shifted only by 0.01 mag in intervening years (see discussion in de Grijs et al. 2014) and thus the absolute scale of the distances has changed a small amount. Thus, the differences between studies can be attributed to the exact parameters and wavelength of the Leavitt Law, treatment of stellar crowding in the photometry, assumptions regarding internal extinction, and assumptions regarding the metallicity term in the Leavitt Law.

Since the LJ12 compilation, additional Cepheid distances have been measured by Mager et al. (2013), Tully et al. (2013), Nataf (2015), and Riess et al. (2016). The distance in Nataf (2015) is not independent because it adopts data from SS11, but performs a test of variant forms of the Milky Way interstellar extinction curve (with a total change $\Delta\mu = 0.06$ mag) and, while the

results are of great interest, we exclude them to avoid overemphasizing SS11 and complicating comparisons.⁸ Similar to the tabulation of LJ12, the distances to M101 via the Leavitt Law span 1 mag, with typical quoted uncertainties at the ~ 0.1 mag level.

5.4. Comparison of Pop I and Pop II Distances to M101

Using the four distances determined from TRGB methods, the weighted mean distance modulus is $\mu_{wt,mean} = 29.11 \pm 0.02$ mag and the unweighted mean distance modulus is $\mu_{mean} = 29.11 \pm 0.03$ mag. These values are plotted in Figure 9a as the vertical dashed and dot-dashed lines, respectively. We note that the “long distances” measured in the S04-field are excluded, as are those from T15 due to a lack of uncertainties (shown in grey in Figure 9a). If we exclude JL17 due to field choice, as previously discussed, then our mean value is determined using the distance modulus in this work and that from SS11, with a result of $\mu_{mean} = 29.08 \text{ mag} \pm 0.02$ (uncertainty weighted).

The weighted mean of 13 distance moduli determined for M101 using the Leavitt Law is $\mu_{wt,mean} = 29.16 \pm 0.02$ mag and the unweighted mean is $\mu_{mean} = 29.16 \pm 0.03$ mag. These values are plotted in Figure 9b as the vertical dashed and dot-dashed lines, respectively. From inspection of Figure 9b, the results before and after 2005 seem to cluster differently. If we limit to only the five distance moduli determined in 2005 and later, the weighted mean is $\mu_{wt,mean} = 29.12 \pm 0.03$ mag and the unweighted mean is $\mu_{mean} = 29.11 \pm 0.05$ mag.

Thus, the “mean” distance to M101 from the Leavitt Law and the TRGB disagree at the $\sim 2\sigma$ -level, though the difference largely depends on what combination of measurements one chooses to compare. The difference is slightly surprising because the absolute scale, in either system, is set in the Large Magellanic Cloud, albeit the SHOES program uses a set of objects to define the absolute scale (see e.g., Riess et al. 2016). We note that in Riess et al. (2016), the calibration of SN2011fe in M101 is an outlier in the calibration relation (their figure 10) and the slightly closer distance measured by the TRGB resolves the discrepancy.

For context, we provide the ranges for distances determined from other standard candles, but note that none of these have comparable precision and accuracy

as either the TRGB- or Cepheid-based scales. Distance moduli determined from the SN Ia, itself, span a range from 28.86 mag to 29.38 mag. Distance moduli determined from the Tully-Fisher relationship span a range from 27.07 mag to 29.62 mag and distance moduli determined from the planetary nebula luminosity function (PNLF) span a range from 29.36 mag to 29.42 mag. Lastly, Carlsten et al. (2019a) presented distances using surface brightness fluctuations to individual satellite galaxies of M101 finding a mean (and median) distance of 6.5 ± 0.12 Mpc ($\mu = 29.10$ mag) with a dispersion of 0.35 Mpc using the nine confirmed M101 satellites. Notably, the surface brightness fluctuation method is, itself, calibrated to the TRGB and galaxies of these low stellar masses typically have small quantities of dust (the full method is described Carlsten et al. 2019b).

6. SUMMARY

In this paper, we have determined the distance modulus to M101 using a carefully selected pointing that is composed of a near pure Population II stars. The methods used in previous works in this series were converted into an end-to-end automated pipeline and produce results of comparable precision and accuracy (Paper II; Paper III; Paper IV; Paper V). We detect the TRGB at $m_{F814W} = 25.04$ mag and determine the statistical and systematic uncertainties to be 0.03 mag and 0.04 mag, respectively. Dereddening the data and using the final CCHP absolute magnitude calibration for the TRGB (Paper VIII), we find a final true distance modulus of $\mu_0 = 29.07 \pm 0.04_{stat} \pm 0.05_{sys}$ mag, which corresponds to a physical distance of $D = 6.52 \pm 0.12_{stat} \pm 0.15_{sys}$ Mpc. The full error budget for this measurement is given in Table 2. This distance is on the low-side of other distances relying on resolved stellar populations (Figure 9), but well within the NED range. Unlike many of the literature methods, our technique is minimally affected from internal extinction and the impact from crowding is negligible.

We have used a set of archival images (Figure 1a and Table 1) to demonstrate that proper selection of a field suitable for TRGB measurement is required to reach high accuracy – even for M101, one of the most nearby SN Ia host galaxies. We demonstrated that while the TRGB discontinuity is visible by eye at the level detected in our CCHP field (e.g., Figure 7), the edge detection algorithm is easily confused due to a combination of multiple stellar populations and multiple structural components. We caution that application of the TRGB in these scenarios will have large uncertainties that may not be encapsulated by commonly applied methods. Though we are able to show that the un-

⁸ In an earlier version of this manuscript posted to ArXiv the Nataf (2015) results were incorrectly presented. The authors apologize sincerely for this error and are thankful that it was corrected before publication.

certainty as measured from the width of the response function does provide a meaningful uncertainty measure in the cases of large effective-smoothing. Additionally, the lower signal-to-noise produces larger magnitude and color uncertainties that amplify confusion by smearing the populations in the luminosity function. We show in Figure 6b that the surface brightness profiles provide insight into the selection of an appropriate pointing free from these contaminating populations, with the combination of all-sky-survey depth *GALEX* and *WISE* imaging being of sufficient quality. If available in the literature, HI maps can also inform field choice to limit the impact from dust.

We warmly thank the anonymous referee for their careful attention to the manuscript that has improved work presented here. We thank Peter Stetson for a copy of the DAOPHOT family of programs as well as his helpful interactions on its use for our science case. RLB thanks Sean Johnson for engaging discussions on gas and dust in the CGM, Saurabh Jha for numerous insights that made their way into this work, and Adam Riess for a helpful discussion of crowding-based systematics. In version of this manuscript posted to ArXiv, the Nataf (2015) results were incorrectly presented. The authors apologize sincerely for this error and are thankful that it was corrected before publication. Support for this work was provided by NASA through Hubble Fellowship grant #51386.01 awarded to R.L.B. by the Space Telescope Science Institute, which is operated by the Association of Universities for Research in Astronomy, Inc., for NASA, under contract NAS 5-26555.

Support for program #13691 was provided by NASA through a grant from the Space Telescope Science Institute, which is operated by the Association of Universi-

ties for Research in Astronomy, Inc., under NASA contract NAS 5-26555. MGL was supported by the National Research Foundation grant funded by the Korean Government (NRF-2017R1A2B4004632). Some of the data presented in this paper were obtained from the Mikulski Archive for Space Telescopes (MAST). STScI is operated by the Association of Universities for Research in Astronomy, Inc., under NASA contract NAS5-26555.

This research has made use of the NASA/IPAC Extragalactic Database (NED) which is operated by the Jet Propulsion Laboratory, California Institute of Technology, under contract with the National Aeronautics and Space Administration.

This research has made use of the NASA/IPAC Infrared Science Archive (IRSA), which is operated by the Jet Propulsion Laboratory, California Institute of Technology, under contract with the National Aeronautics and Space Administration.

This work made use of THINGS, ‘*The HI nearby Galaxy Survey*’ (Walter et al. 2008). Available: <http://www.mpia.de/THINGS/Overview.html>

This publication makes use of data products from the Wide-field Infrared Survey Explorer, which is a joint project of the University of California, Los Angeles, and the Jet Propulsion Laboratory/California Institute of Technology, funded by the National Aeronautics and Space Administration.

Based on observations made with the NASA Galaxy Evolution Explorer. *GALEX* is operated for NASA by the California Institute of Technology under NASA contract NAS5-98034.

Facilities: HST (ACS/WFC)

Software: DAOPHOT (Stetson 1987), ALLFRAME (Stetson 1994)

REFERENCES

- Alves, D. R., & Cook, K. H. 1995, *AJ*, 110, 192
- Anand, G. S., Rizzi, L., & Tully, R. B. 2018, *AJ*, 156, 105
- Beaton, R. L., Freedman, W. L., Madore, B. F., et al. 2016, *ApJ*, 832, 210
- Beaton, R. L., Bono, G., Braga, V. F., et al. 2018, *SSRv*, 214, 113
- Bohlin, R. C. 2016, *AJ*, 152, 60
- Calzetti, D. 2013, LEGUS: Legacy ExtraGalactic UV Survey, HST Proposal, ,
- Cardelli, J. A., Clayton, G. C., & Mathis, J. S. 1989, *ApJ*, 345, 245
- Carlsten, S. G., Beaton, R. L., Greco, J. P., & Greene, J. E. 2019a, *ApJL*, 878, L16
- . 2019b, *ApJ*, 879, 13
- Carraro, G. 2015, *Boletin de la Asociacion Argentina de Astronomia La Plata Argentina*, 57, 138
- Cook, K. H., Aaronson, M., & Illingworth, G. 1986, *ApJL*, 301, L45
- Cook, K. H., Aaronson, M., & Illingworth, G. 1989, in *BAAS*, Vol. 21, *Bulletin of the American Astronomical Society*, 719
- de Grijs, R., Wicker, J. E., & Bono, G. 2014, *AJ*, 147, 122
- Dolphin, A. E. 2000a, *PASP*, 112, 1383
- . 2000b, *PASP*, 112, 1397
- Ferrarese, L., Mould, J. R., Kennicutt, Jr., R. C., et al. 2000, *ApJ*, 529, 745

- Freedman, W. 2014, CHP-II: The Carnegie Hubble Program to Measure Ho to 3% Using Population II, HST Proposal, ,
- Freedman, W. L. 2017, *Nature Astronomy*, 1, 0121
- Freedman, W. L., & Madore, B. F. 2010, *ARA&A*, 48, 673
- Freedman, W. L., Madore, B. F., Scowcroft, V., et al. 2012, *ApJ*, 758, 24
- Freedman, W. L., Madore, B. F., Gibson, B. K., et al. 2001, *ApJ*, 553, 47
- Freedman, W. L., Madore, B. F., Hatt, D., et al. 2019, arXiv e-prints, arXiv:1907.05922
- Gil de Paz, A., Boissier, S., Madore, B. F., et al. 2007, *ApJS*, 173, 185
- Hatt, D., Beaton, R. L., Freedman, W. L., et al. 2017, *ApJ*, 845, 146
- Hatt, D., Freedman, W. L., Madore, B. F., et al. 2018a, *ApJ*, 861, 104
- . 2018b, *ApJ*, 866, 145
- Hill, R. J., Ferrarese, L., Stetson, P. B., et al. 1998, *ApJ*, 496, 648
- Hoyt, T. J., Freedman, W. L., Madore, B. F., et al. 2018, *ApJ*, 858, 12
- . 2019, arXiv e-prints, arXiv:1907.05891
- Jacobs, B. A., Rizzi, L., Tully, R. B., et al. 2009, *AJ*, 138, 332
- Jang, I. S., & Lee, M. G. 2017a, *ApJ*, 836, 74
- . 2017b, *ApJ*, 835, 28
- Jang, I. S., Hatt, D., Beaton, R. L., et al. 2018, *ApJ*, 852, 60
- Kelson, D. D., Illingworth, G. D., Freedman, W. F., et al. 1996, *ApJ*, 463, 26
- Kennicutt, Jr., R. C., Stetson, P. B., Saha, A., et al. 1998, *ApJ*, 498, 181
- Krist, J. E., Hook, R. N., & Stoehr, F. 2011, in *Proc. SPIE*, Vol. 8127, *Optical Modeling and Performance Predictions V*, 81270J
- Lee, M. G., Freedman, W. L., & Madore, B. F. 1993, *ApJ*, 417, 553
- Lee, M. G., & Jang, I. S. 2012, *ApJL*, 760, L14
- Mack, J., Gilliland, R. L., Anderson, J., & Sirianni, M. 2007, *WFC Zeropoints at -80C*, Tech. rep.
- Macri, L. M., Calzetti, D., Freedman, W. L., et al. 2001, *ApJ*, 549, 721
- Madore, B. F., & Freedman, W. L. 1995, *AJ*, 109, 1645
- Madore, B. F., & Freedman, W. L. 1999, in *Astronomical Society of the Pacific Conference Series*, Vol. 167, *Harmonizing Cosmic Distance Scales in a Post-HIPPARCOS Era*, ed. D. Egret & A. Heck, 161–174
- Madore, B. F., Mager, V., & Freedman, W. L. 2009, *ApJ*, 690, 389
- Madore, B. F., Freedman, W. L., Hatt, D., et al. 2018, *ApJ*, 858, 11
- Mager, V. A., Madore, B. F., & Freedman, W. L. 2008, *ApJ*, 689, 721
- . 2013, *ApJ*, 777, 79
- Makarov, D., Makarova, L., Rizzi, L., et al. 2006, *AJ*, 132, 2729
- McQuinn, K. B. W., Skillman, E. D., Dolphin, A. E., Berg, D., & Kennicutt, R. 2016a, *ApJ*, 826, 21
- . 2016b, *AJ*, 152, 144
- . 2017, *AJ*, 154, 51
- Méndez, B., Davis, M., Moustakas, J., et al. 2002, *AJ*, 124, 213
- Monson, A. J., Beaton, R. L., Scowcroft, V., et al. 2017, *AJ*, 153, 96
- Nataf, D. M. 2015, *MNRAS*, 449, 1171
- Newman, J. A., Ferrarese, L., Stetson, P. B., et al. 2001, *ApJ*, 553, 562
- Nugent, P., Sullivan, M., Bersier, D., et al. 2011a, *The Astronomer’s Telegram*, 3581
- Nugent, P. E., Sullivan, M., Cenko, S. B., et al. 2011b, *Nature*, 480, 344
- Overbye, D. 1991, *Lonely hearts of the cosmos. The scientific quest for the secret of the universe.*
- Paturel, G., Teerikorpi, P., Theureau, G., et al. 2002, *A&A*, 389, 19
- Peek, J. E. G., Ménard, B., & Corrales, L. 2015, *ApJ*, 813, 7
- Persson, S. E., Madore, B. F., Krzemiński, W., et al. 2004, *AJ*, 128, 2239
- Riess, A. G., Casertano, S., Yuan, W., Macri, L. M., & Scolnic, D. 2019, *ApJ*, 876, 85
- Riess, A. G., Macri, L., Casertano, S., et al. 2011, *ApJ*, 730, 119
- Riess, A. G., Macri, L. M., Hoffmann, S. L., et al. 2016, *ApJ*, 826, 56
- Riess, A. G., Casertano, S., Yuan, W., et al. 2018, arXiv e-prints, arXiv:1801.01120
- Rizzi, L., Tully, R. B., Makarov, D., et al. 2007, *ApJ*, 661, 815
- Saha, A., Thim, F., Tammann, G. A., Reindl, B., & Sandage, A. 2006, *ApJS*, 165, 108
- Sakai, S., Ferrarese, L., Kennicutt, Jr., R. C., & Saha, A. 2004, *ApJ*, 608, 42
- Sandage, A., & Tammann, G. A. 1974, *ApJ*, 194, 223
- Schlafly, E. F., & Finkbeiner, D. P. 2011, *ApJ*, 737, 103
- Schlegel, D. J., Finkbeiner, D. P., & Davis, M. 1998, *ApJ*, 500, 525
- Serenelli, A., Weiss, A., Cassisi, S., Salaris, M., & Pietrinferni, A. 2017, *A&A*, 606, A33

- Shappee, B. 2014, Whimper of a Bang: Documenting the Final Days of the Nearby Type Ia Supernova 2011fe, HST Proposal, ,
- . 2015, Whimper of a Bang: Documenting the Final Days of the Nearby Type Ia Supernova 2011fe, HST Proposal, ,
- Shappee, B. J., & Stanek, K. Z. 2011, ApJ, 733, 124
- Shappee, B. J., Stanek, K. Z., Kochanek, C. S., & Garnavich, P. M. 2016, ArXiv e-prints, arXiv:1608.01155
- Sirianni, M., Jee, M. J., Benitez, N., et al. 2005, PASP, 117, 1049
- Steer, I., Madore, B. F., Mazzarella, J. M., et al. 2017, AJ, 153, 37
- Stetson, P. B. 1987, PASP, 99, 191
- . 1990, PASP, 102, 932
- . 1994, PASP, 106, 250
- Stetson, P. B., & Harris, W. E. 1988, AJ, 96, 909
- Stetson, P. B., Saha, A., Ferrarese, L., et al. 1998, ApJ, 508, 491
- Tikhonov, N. A., Lebedev, V. S., & Galazutdinova, O. A. 2015, Astronomy Letters, 41, 239
- Tully, R. B., Courtois, H. M., Dolphin, A. E., et al. 2013, AJ, 146, 86
- Walter, F., Brinks, E., de Blok, W. J. G., et al. 2008, AJ, 136, 2563
- Willick, J. A., & Batra, P. 2001, ApJ, 548, 564
- Zaritsky, D. 1994, AJ, 108, 1619

APPENDIX

A. SUPPLEMENTARY INFORMATION

In this Appendix, we provide additional information regarding the photometry and analyses undertaken in the main text for the benefit of the reader and for reproducibility of the results.

A.1. *Photometric Terms for Each Field*

Table 3 presents the time dependent zeropoint (ZP), correction to an infinite aperture (APInf), and aperture core correction (ApCore_{c1} for chip1 and ApCore_{c2} for chip2) used for each of the *HST* +ACS pointings in M 101. The STSci provided values (ZP and APInf) are sometimes adjusted retroactively at the $\sim 1\%$ level and these changes are not negligible for the precisions quoted here. The APCore correction in Table 3 is the mean value for the series of frames to give a sense of the correction. The values used for the photometry in the main text are applied on a frame-by-frame basis before computing the mean of the frame-by-frame instrumental magnitudes.

A.2. *Image Quality and Magnitude Uncertainty Cuts for Each Field*

The photometry used in the main text is restricted using the photometric uncertainty (σ_{F814W}), the sharpness parameter (sharp_{F814W}), and the chi parameter (χ_{F814W}) that are reported by DAOPHOT. We use a set of functions to fit the form of the distributions for these parameters as a function of magnitude and define likely stellar sources to be those that pass all three tests. The functions follow the following forms:

$$\sigma_{F814W} < 0.03 + 0.003 \times e^{m-m_\sigma}, \quad (\text{A1})$$

$$|\text{sharp}_{F814W}| < 0.10 + 0.0075 \times e^{m-m_{\text{sharp}}}, \quad (\text{A2})$$

$$\chi_{F814W} < 2.0 + e^{m-m_\chi}, \quad (\text{A3})$$

where the m_σ , m_{sharp} , and m_χ are determined for each field individually and generally scale with signal-to-noise. The value for each parameter are given for each field in Table 3.

The results of applying these cuts are given in the panels of Figure 10 for each of the fields, with the CCHP field reproduced for ease of inter comparison (Figure 10i). As anticipated from the shorter exposure times (Table 1), the quality parameters show an upturn in σ_{F814W} and a flaring in sharp_{F814W} at a brighter magnitude. The χ_{F814W} shows similar behavior for all panels. These restrictions were employed for all of the visualizations of the photometry presented in the main text as well as all of the analyses undertaken with these data.

A.3. *Color-Magnitude Selection Box*

The color magnitude selection box (blue shading in Figure 4) that were applied to the color-magnitude data before building the luminosity functions is defined as follows:

$$\begin{aligned} m_{F814W} &\geq -6.0 (m_{F814W} - m_{F606W} - 1.0) + 25.10 \\ m_{F814W} &\leq -6.0 (m_{F814W} - m_{F606W} - 1.6) + 25.10 \end{aligned} \quad (\text{A4})$$

The slope of $-6.0 \text{ mag color}^{-1}$ was measured from high signal-to-noise photometry for Local Group galaxies used in the RR Lyrae arm of the CCHP Paper I. The color-width of 0.6 mag was set based on the width of the RGB in Figure 4i. The data were also restricted to the color and magnitude ranges of the color-magnitude plot to avoid any confusion over differences between Figure 4i and Figure 4ii. Equation A4 was transformed into the the F555W-F814W color-system following Equation 3 to set the equivalent color-range.

A.4. *Full Visualizations for Archival Fields*

The full visualization akin to Figure 5 is provided for each of the archival fields is provided in the panels of Figure 5. More specifically, the a-subpanels have the LF plotted for a range of smoothing widths (σ_s), the b-subpanels have the edge response (η) for that same range of smoothing widths, the c-panels are zooms of the normalized η around η_{max} for a subset of σ_s , and the d-panels demonstrate different means of quantifying the uncertainty on the determination of $m_{\eta_{max}}$.

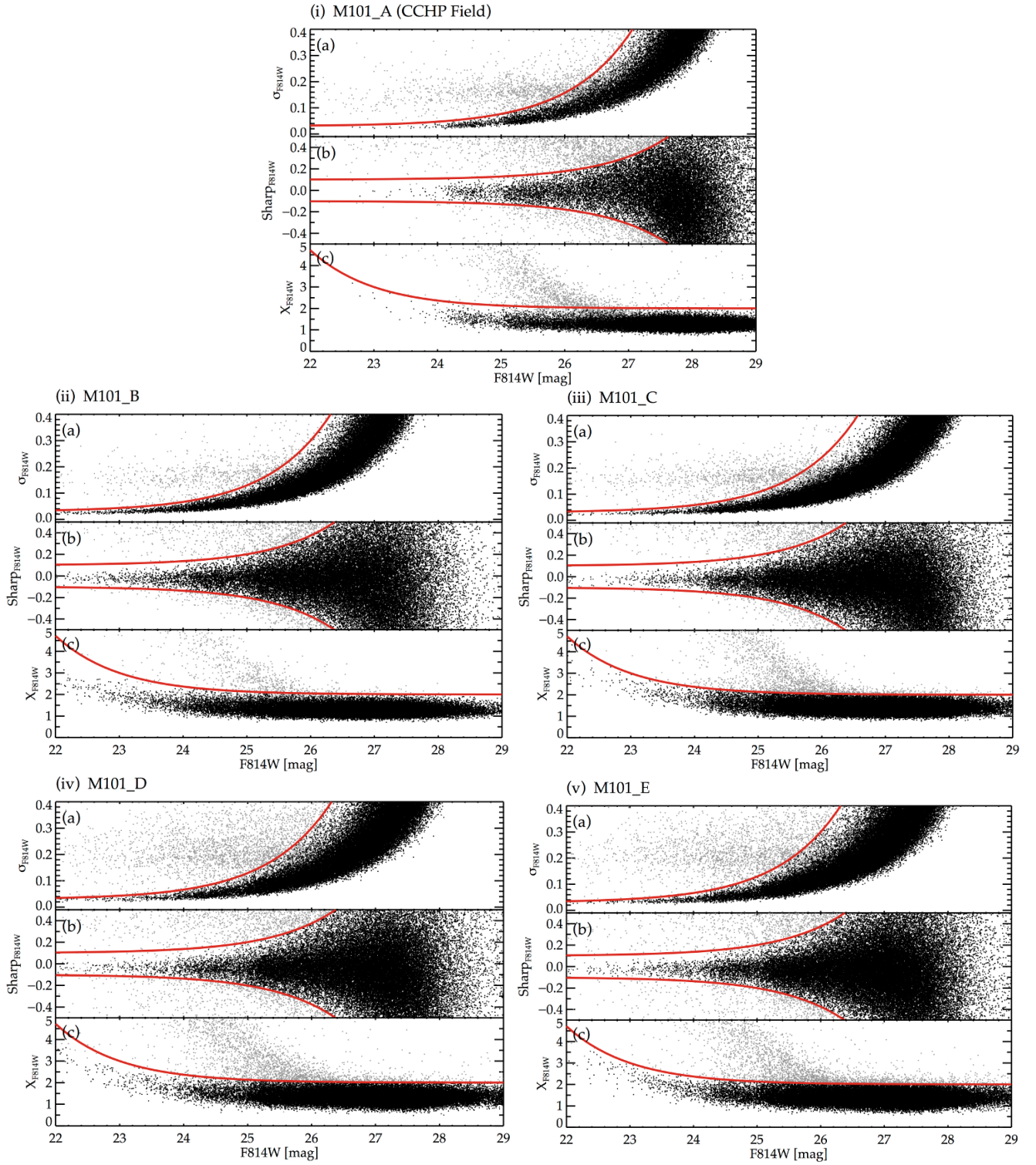


Figure 10. Photometry quality diagrams for (i) M101_A (CCHP field) and the four archival fields (ii) M101_B, (iii) M101_C, (iv) M101_D, and (v) M101_E. The sub-panels demonstrate (a) the photometric uncertainty and image quality metrics (b) sharpness parameter and (c) χ as a function of the F814W magnitude. The restrictions used on the photometry are shown in red with the sources passing all of the restrictions in black and the sources not passing any one criterion in gray. Generally, the archival fields are slightly shallower than our CCHP pointing, but are similar in signal-to-noise as observations in other SN Ia-hosts in the CCHP program.

Table 3. Quantities Applied to the Photometry

Quantity	M101_A	M101_B	M101_C	M101_D	M101_E
Observation Date	2015-09-09	2014-10-09	2016-02-19	2013-10-18	2014-02-15
ZP F555W	...	25.721(± 0.02)	25.720(± 0.02)
APInf F555W	...	0.096(± 0.02)	0.096(± 0.02)
ApCore _{c1} F555W	...	-0.004(± 0.012)	0.035(± 0.033)
ApCore _{c2} F555W	...	-0.044(± 0.025)	-0.021(± 0.016)
ZP F606W	26.411(± 0.02)	26.413(± 0.02)	26.413(± 0.02)
APInf F606W	0.095(± 0.02)	0.095(± 0.02)	0.095(± 0.02)
ApCore _{c1} F606W	0.007(± 0.042)	0.065(± 0.035)	0.006(± 0.033)
ApCore _{c2} F606W	-0.056(± 0.036)	0.022(± 0.037)	-0.023(± 0.019)
ZP F814W	25.523(± 0.02)	25.524(± 0.02)	25.523(± 0.02)	25.524(± 0.02)	25.524(± 0.02)
APInf F814W	0.098(± 0.02)	0.098(± 0.02)	0.098(± 0.02)	0.098(± 0.02)	0.098(± 0.02)
ApCore _{c1} F814W	0.101(± 0.024)	0.074(± 0.006)	0.067(± 0.008)	0.063(± 0.008)	0.049(± 0.019)
ApCore _{c2} F814W	0.063(± 0.020)	0.044(± 0.006)	0.050(± 0.005)	0.056(± 0.013)	0.061(± 0.013)
$A_{I,MW}$ [mag]	0.02(± 0.01)	0.01(± 0.01)	0.01(± 0.01)	0.01(± 0.01)	0.01(± 0.01)
m_σ [mag]	22.25	21.50	21.75	21.50	21.50
m_{sharp} [mag]	23.75	22.50	22.50	22.50	22.50
m_χ [mag]	23.00	23.00	23.00	23.00	23.00

A.5. Measurement of TRGB in M101_E

The M101_E field is the same image dataset used by JL17. To facilitate comparison between the JL17 result and our own, we have performed a more detailed analysis of this field to the same level as for our CCHP field (M101_A).

Thus, identical procedures were followed as for the CCHP Field and the supporting figures are given here for completeness. The ASLF were constructed, inserted into the images, photometered, and analyzed. The panels of Figure 12 give the steps of this process; more specifically, Figure 12a shows the input and output LF, Figure 12b summarizes the statistical, systematic and total uncertainties for each σ_s , and Figure 12c provides the distribution of TRGB measurements for the selected σ_s from which the final uncertainties are adopted. The resulting σ_s is 0.05 mag, identical to that of the CCHP Field and the uncertainties are similar, with 0.03 mag and 0.04 mag for the statistical and systematic uncertainties, respectively.

We note, however, that our ASLF analysis here is somewhat superficial given our knowledge of the field. More specifically, we have only modeled, effectively, a single stellar population; whereas it is evident from the CMD that the M101_E contains many different populations (e.g., stellar sequences of different ages and metallicities) that are superimposed as part of different galactic structures (with different internal extinctions that shift the apparent distance). With this in mind, we suspect that our estimated uncertainties on the TRGB detection should be taken as lower limits on the true uncertainties.

The panels of Figure 12 demonstrate the TRGB detection. The CMD is given in Figure 12i, with the blue shading giving a color-selection box that is broadened from that in Figure 4i proportional to the photometric uncertainties. Figure 12ii gives the LF in both its raw and GLOESS smoothed form. Figure 12iii is the response function of the Sobel kernel showing a clear peak at 25.105 ± 0.03 mag, with the quoted uncertainty being the statistical uncertainty on the TRGB detection.

A.6. Literature Distances to M 101

Table 4 gives the individual values, uncertainties, references and notes for the distances to M 101 that were used to construct Figure 9.

Table 4. Literature Distances to M 101

Measurement of the TRGB		
Study	TRGB Magnitude (F814W)	Notes
Sakai et al. (2004) (S04)	25.40 ± 0.04	
Rizzi et al. (2007) (R07)	25.31 ± 0.08	
Shappee & Stanek (2011) (SS11)	25.00 ± 0.06	
Lee & Jang (2012) (LJ12)	25.28 ± 0.01	Concerns over photometric zero point.
Tikhonov et al. (2015) (T15)	25.05	no uncertainties given
	25.10	Pointing 1; no uncertainties given
	25.11	Field M101_D; no uncertainties given
Jang & Lee (2017a) (JL17)	25.16 ± 0.04	
EDD (Jacobs et al. 2009)	$25.08 +0.02 -0.03$	Independent reduction of CCHP Pointing
CCHP (This Work)	25.04 ± 0.03	
Distances determined via the LEAVITT LAW		
Study	Distance Modulus	Notes
Kelson et al. (1996)	29.24 ± 0.10	
Stetson et al. (1998)	29.05 ± 0.14	
	29.21 ± 0.17	
Kennicutt et al. (1998)	29.20 ± 0.07	
	29.34 ± 0.08	
	29.39 ± 0.07	
Ferrarese et al. (2000)	29.34 ± 0.10	
Macri et al. (2001)	29.04 ± 0.08	NIR using <i>HST</i> + NICMOS
	29.77 ± 0.09	
	29.58 ± 0.09	
	29.45 ± 0.08	
	29.37 ± 0.01	
Newman et al. (2001)	29.06 ± 0.11	
	29.16 ± 0.09	
Willick & Batra (2001)	29.21 ± 0.08	
Freedman et al. (2001) (KP)	29.13 ± 0.11	Final KP Result
Paturel et al. (2002)	29.23 ± 0.07	$\mu_{LMC} = 18.37$ mag
	29.26 ± 0.15	
	29.30 ± 0.07	
Sakai et al. (2004)	29.14 ± 0.09	
	29.24 ± 0.08	
Saha et al. (2006)	29.18 ± 0.08	$\mu_{LMC} = 18.54$ mag
Shappee & Stanek (2011) (SS11)	29.04 ± 0.04	$\mu_{LMC} = 18.41$ mag
Mager et al. (2013)	28.96 ± 0.11	$\mu_{LMC} = 18.48$ mag
Tully et al. (2013)	29.21 ± 0.06	Cosmicflows-2 Compilation
Nataf (2015)	29.20 ± 0.03	Uses SS11, but $A_I/E(V-I)=1.1450$; $\Delta\mu_{LMC}=10.72 \pm 0.03$ mag
Riess et al. (2016)	29.14 ± 0.05	

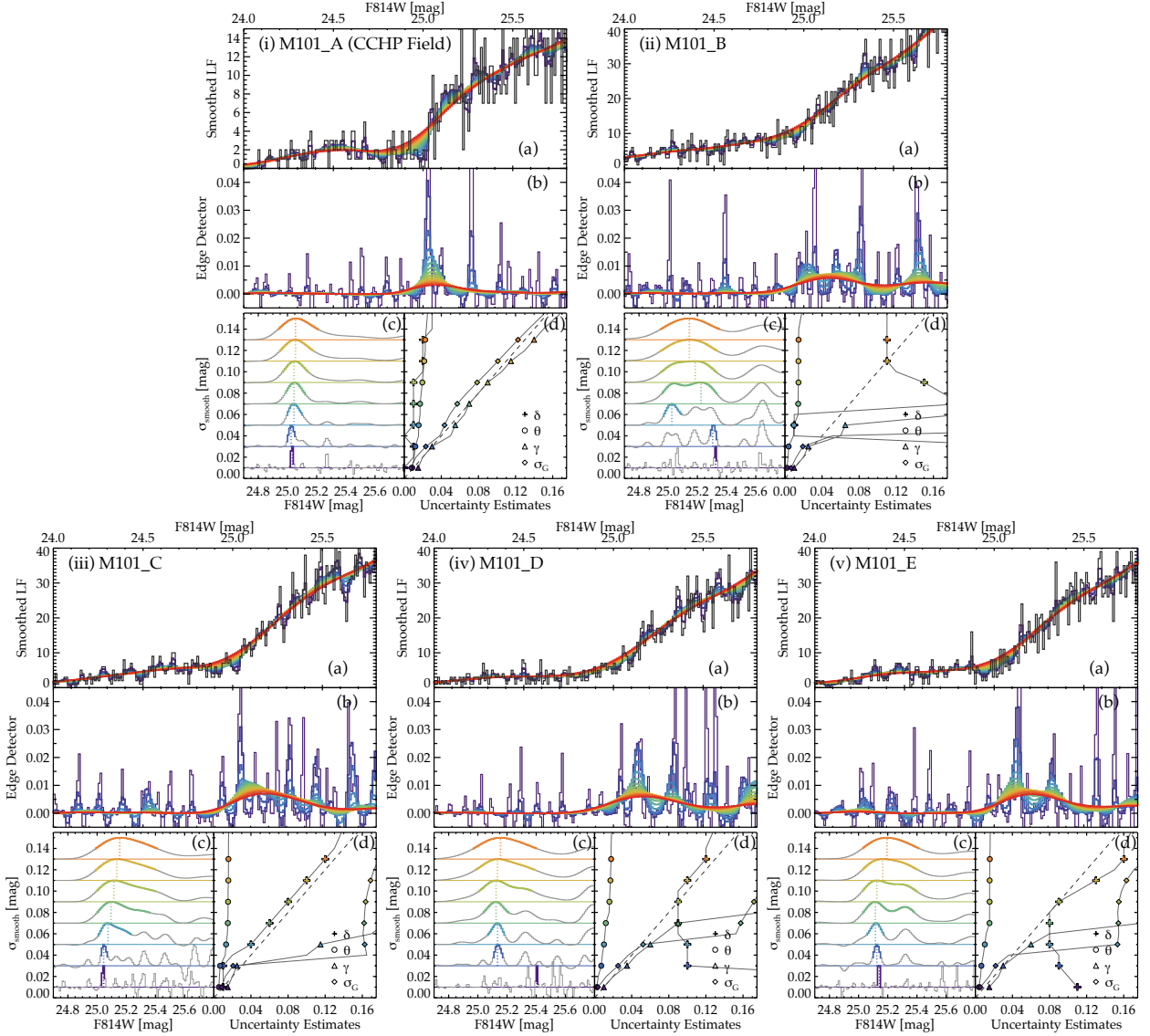


Figure 11. The impact of smoothing the luminosity function on TRGB measurements. Each panel is for an individual field, as follows: (i) M101-A (CCHP Field), (ii) M101-B, (iii) M101-C, (iv) M101-D, and (v) M101-E. The sub-panels are identical to that of Figure 5 and the panel for M101-A is repeated for ease of comparison. While the LF (a-subpanels) do not show obvious differences, the edge-response (η) shows more complex behavior than in M101-A (b-subpanels), which when normalized (c-subpanels) show that there is great ambiguity in the determination of η_{max} . The statistical metrics explored for M101-A (d-subpanels) are complex and difficult to parse. We conclude that, unlike the CCHP field, the archival fields do not show a clear TRGB measurement.

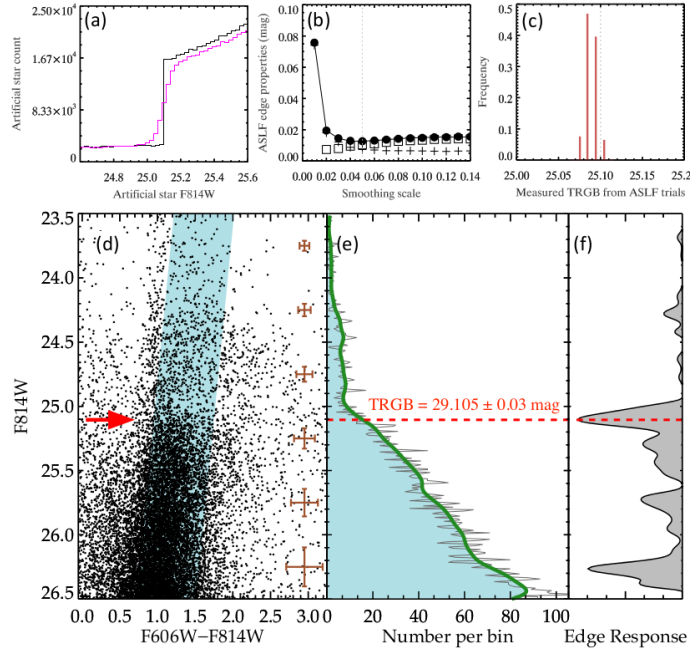


Figure 12. Summary of the ASLF procedure to determine the optimal σ_s and its measurement uncertainties for the M101_E field (a-c) and the TRGB measurement in the M101_E field (d-f). (a) A comparison of the input (black) and output (purple) ASLF – note that only the AGB and RGB are modeled here. (b) The systematic (open box), statistical (plus), and quadratic sum (filled circle) uncertainties determined via TRGB measurements of 10,000 realizations of the ASLF to match our source counts. (c) The distribution of TRGB measurements for the “optimal” σ_s of 0.05 mag. These uncertainties are smaller than those in M101_A (Figure 3) due to the larger number of sources. Due to the simplicity of our modeling (only AGB + RGB) and the complexity of the field, we suspect these uncertainties should only be considered a lower limit on the true uncertainties. (d) CMD and a color-cut (blue-shaded region) similar to that used in the CCHP field. (e) Raw LF binned at 0.01 mag (thin gray) and GLOESS smoothed LF using $\sigma_s = 0.05$ mag (thick green). (f) Edge detection response function with a maximum at 29.105 ± 0.03 mag.